Stick-slip vs. stable sliding fault behaviour: A case-study using a multidisciplinary approach in the volcanic region of Mt. Etna (Italy)

R. Azzaro*, A. Bonforte, S. D'Amico, F. Guglielmino, L. Scarfì

Istituto Nazionale di Geofisica e Vulcanologia, Osservatorio Etneo, piazza Roma 2, 95125 Catania, Italy

A B S T R A C T

In active volcanic zones, fault dynamics is considerably fast but it is often difficult to separate the pattern of nearly continuous large-scale volcanic processes (inflation/deflation processes, flank instability) from impulsive episodes such as dyke intrusions or coseismic fault displacements. At Etna, multidisciplinary studies on active faults whose activity does not strictly depend on volcanic processes, are relatively few. Here we present the case-study of the San Leonardello fault, an active structure located in the eastern flank of Mt. Etna characterised by a well-known seismic history. This fault saw renewed activity in May 2009, when pre-seismic creeping along the southern segment preceded an M_W 4.0 earthquake in the northern segment, followed by some twenty-five aftershocks. Later, in March–April 2016, creep events reactivated the southern section of the same fault. Both the seismic and aseismic phenomena were recorded by the seismic and GNSS networks of INGV-Osservatorio Etneo, and produced surface faulting that left a footprint in the pattern of ground deformation detected by the InSAR measurements. We demonstrate that the integration of multidisciplinary data collected for volcano surveillance may shed light on different aspects of fault dynamics, and allow understanding how coseismic slip and creep alternate in space and time along the strike. Moreover, we use findings from our independent datasets to propose a conceptual model of the San Leonardello fault, taking into account behaviour and previous constraints from fault-based seismic hazard analyses. Although the faulting mechanisms described here occur at a very small scale compared with those of a purely tectonic setting, this case-study may represent a perfect natural lab for improving knowledge of seismogenic processes, also in other fault zones characterised by stick slip vs. stable-sliding fault behaviour.

1. Introduction

Multidisciplinary studies aimed at modelling behaviour of active faults are commonly applied in tectonic domains, often in the aftermath of a large earthquake, by integrating seismological data and geodetic measurements and, if surface faulting occurs, considering field observations as well. The data acquired during a seismic sequence allows obtaining a comprehensive picture on the process of seismic rupture, though the overall dynamics of the source is complicated by the role played by the heterogeneous behaviour of the shallow crust (not a purely elastic-brittle rheology) as well as by the aseismic deformation. Fault creep is increasingly recognised as an essential part of the seismogenic process but it presents a variety of complex situations both in terms of scale and occurrence of phenomena (Thomas et al., 2014; Avouac, 2015; Harris, 2017, and references therein). The most explanatory studies on seismogenic vs. aseismic fault behaviour usually regard crustal fault zones where strain and moment rates released overall are very high, typically along major continental faults or at boundary plates (thrust-faulting) (e.g. Lee et al., 2003; Lindsey et al., 2014).

On the other hand, faults at Etna display the two end-member modes of rupture mechanism (Lo Giudice and Rasà, 1992; Azzaro, 2004), with different sections of the same fault displaying displacement histories governed by stick-slip behaviour (earthquake-related slip on seismogenic faults) or stable-sliding behaviour (aseismic slip on creeping faults). Field observations indicate that fault creep (Rasà et al., 1996) occurs as a near-continuous long-period, low slip-rate movement punctuated by prominent displacement episodes, known in the literature as creep events (e.g. Wesson, 1988). These spasmodic, short-lived displacements may accompany the seismic activity along the same fault, in the form of pre- and post-seismic slip, or be associated with local geodynamic processes (Mattia et al., 2015; Palano, 2016), also in connection with magmatic (i.e. dyke) intrusions (Puglisi et al., 2008; Le Corvec et al., 2014).

---

* Corresponding author.
   E-mail address: raffaele.azzaro@ingv.it (R. Azzaro).

Investigating fault activity in volcanic zones may be an advantage since the dynamics is usually faster than in most tectonic environments. Nonetheless, there are complexities deriving from the difficulty in separating the pattern of nearly continuous volcanic processes - phases of inflation or deflation of the volcano due to volume variations in the magma storage, asymmetrical deformation related with dyke intrusions or flank instability processes - from the impulsive episodes such as coseismic fault displacements. At Etna, analyses on tectonic features have been obtained since the use of SAR generation satellite data (Borgia et al., 2000; Froger et al., 2001; Lundgren et al., 2004; Bonforte et al., 2011) but, apart from the huge literature on models investigating volcano dynamics as a whole (Solaro et al., 2010; Poland et al., 2017, and references therein), specific studies on individual faults are comparatively few (Azzaro et al., 2001; Bonforte et al., 2007, 2013b; Gambino et al., 2011; Currenti et al., 2010, 2012; Alparone et al., 2013a, 2013b; Bonaccorso et al., 2013). Among them, the availability of multidisciplinary data for analysing fault dynamics in connection with significant earthquakes and surface faulting remains quite rare at Etna, being limited to only a few cases (Obrizzo et al., 2001; Guglielmino et al., 2011; Ruch et al., 2013; Bonforte et al., 2019; De Novellis et al., 2019).

In this paper, we present the results of a multidisciplinary analysis aimed at modelling the San Leonardello fault, an active volcano-tectonic feature located in the lower eastern flank of Mt. Etna. Characterised by a well-known seismic history over a centennial time-span and fault behaviour, this structure saw renewed activity in May 2009, when pre-seismic creeping along the southern segment of the fault preceded an M_W 4.0 earthquake in the northern segment, followed by some twenty-five aftershocks rupturing the same fault section. Later, in March–April 2016, creep events reactivated the southern segment of the fault. Both the seismic and aseismic phenomena produced surface faulting, and were recorded by the seismic and GNSS networks of INGV-Osservatorio Etneo. Fault slip also left a clear footprint in the pattern of ground deformation detected by InSAR measurements.

These different typologies of data have been analysed and correlated in order to constrain a geometric-kinematic model of the S. Leonardello fault and to determine its behaviour, previously defined on the basis of field observations alone. Although the faulting mechanisms described here occur at a very small scale compared with those of a purely tectonic setting, this case-study may represent a perfect natural lab for improving our basic knowledge of seismogenic processes also in other fault zones characterised by stick-slip vs. stable-sliding fault behaviour.

2. Background setting

2.1. Structural and seismotectonic outline of the eastern flank of Etna

Mount Etna is a 3300 m high basaltic strato-volcano built up over the past 500 ka on the eastern coast of Sicily in a geodynamic setting generated during the Neogene convergence between the African and European plates (Fig. 1a) (Branca et al., 2011; Polonia et al., 2016). Its structural framework and local-scale geodynamics are the result of a complex interaction between regional tectonics and volcano-related processes, the latter typically governed by flank instability and magma-induced movements (Azzaro et al., 2013a; Bonforte et al., 2013a; Le Corvec et al., 2014; Urlaub et al., 2018, and references therein). In brief, the structural limits between the unstable, E-ESE seaward sliding sector of the volcano and the steady sedimentary areas is represented to the north by the Pernicana fault (PF in Fig. 1), a 20 km long sinistral strike-slip structure featuring a complex behaviour and slip rate variability also in connection with the volcanic activity (Bonaccorso et al., 2013; D'Amato et al., 2017), and to the south by a system of dextral-oblique tectonic structures, the Tremestieri-Trecastagni-San Gregorio faults (TMF-TCF-SG in Fig. 1) (Bonforte et al., 2011; Azzaro et al., 2012 and references therein; Barreca et al., 2013).

The eastern flank of Etna is crossed by the Timpe fault system (TFS in Fig. 1), a prominent tectonic feature consisting of a 20 km long belt of mainly extensional structures arranged as parallel east-facing step-faults (Fig. 2a), locally interrupted by antithetic structures forming narrow grabens. TFS is segmented into individual steep fault escarpments whose intense tectonic activity is indicated by fresh morphological landforms (Azzaro et al., 2012) as well as by the structural control on the drainage pattern (Monaco et al., 1997).

Overall TFS moves with slip-rates ranging from 2 to 4 mm/yr and, like other faults at Etna, has complex dynamics characterised by locked fault segments (i.e. seismogenic) vs. creeping ones (see Fig. 1) (Azzaro, 2004). From the seismogenic point of view, the Timpe faults represent the sources responsible for the strongest earthquakes known to have occurred at Etna in the last centuries (1865, 1879, 1911, 1914). It is a volcano-tectonic seismicity characterised by recurrent shallow events, with magnitude generally not exceeding $M_L \sim 5.0$ but capable of producing heavy damage and even destruction in areas of a limited extent; the thickness of the seismogenic layer is typically lesser than 5 km in this area (Azzaro et al., 2017), differently from the overall focal depth distribution in the Etna region (Alparone et al., 2015). Many earthquakes are also accompanied by coseismic surface faulting (Azzaro, 1999). The significance of this dense network of highly active seismogenic faults in terms of hazard is relevant, as they cross a very urbanized sector of the volcano and determine the same level of shaking expected by the large regional earthquakes, but in shorter exposure times (e.g. 10–30 years; see Azzaro et al., 2013b). The role of the site-specific response (amplification factors) as well as of topography in hazard computations, is significant for this flank of the volcano as demonstrated in Peruzza et al. (2017).

2.2. The San Leonardello fault

The San Leonardello fault (SLF) exhibits an exposed scarp extending for 9 km with a NNW-SSE trend from the coastline to the south as far as the outskirts of the village of Macchia (Fig. 2). Like other nearby structures, the morphotectonic evidence appears greater along its northern section (Fig. 2b), where the vertical offset of 35 m is accommodated by an exposed fault scarp and the relevant component of extension produces a narrow but impressive graben in the footwall block, measuring 90 m in width and 2 km in length (it is the most prominent feature at Etna, *g* in Fig. 2). The southern section of SLF continues as an individual steep escarpment, progressively diminishing to 10–6 m in height and gently curving at the southernmost termination in the N-S direction (Azzaro et al., 2012). At San Leonardello, a hamlet located in the central section of SLF, the fault branches out into two splay faults that connect with the Macchia fault (MCF); there is a third splay fault at the northern tip of SLF.

MCF represents an antithetic fault of SLF, defining an 800 m wide graben-like feature in-between (Fig. 2c). It develops with the same trend for ca. 8 km from Pozzillo to San Giovanni Montebello with a west-dipping exposed fault scarp up to 40 m high except in the central section, where the fault trace disappears buried under a basin fill but also in part concealed under the urban area of San Matteo.

Regarding fault behaviour, SLF shows different features along strike (Azzaro, 2004). The northern segment is seismogenic and extends between the villages of Macchia and San Leonardello (Fig. 2). Its seismic history, known since the late 1800s, is characterised by some major earthquakes with magnitude M_L ranging from 3.4 to 4.0 (Fig. 3), which have produced damage with macroseismic effects reaching intensities up to the VII-VIII degree on the European Macroseismic Scale (hereafter EMS, see Grünthal, 1998). These events were also accompanied by evident coseismic surface faulting along the same fault segment, with end-to-end ruptures up to 4 km in length (Azzaro, 1999). Conversely, the southern segment extending from San Leonardello as far as the coast shows field evidence of a continuous, aseismic fault displacement. The mean creep-rate calculated by the offset of man-made features astride
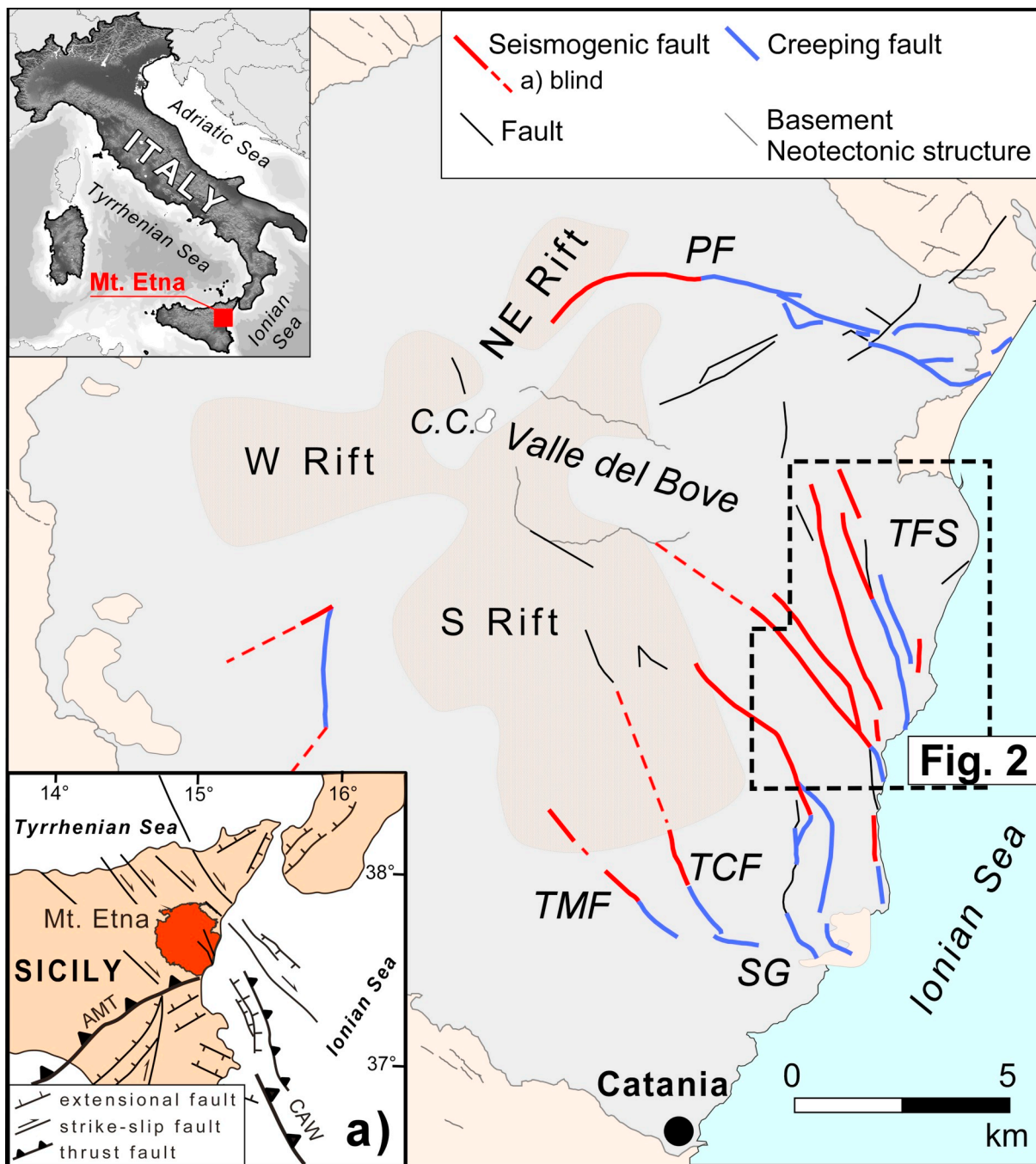
Fig. 1. Seismotectonic model of active faults in the Mt. Etna region (from Azzaro et al., 2012). Volcanic products are denoted by the grey area overlying un-distinguished sedimentary and metamorphic basement. Fault abbreviations: PF, Pernicana; SG, San Gregorio; TFS, Timpe fault system; TCF, Trecastagni; TMF, Tremestieri. The main active, rift zones are also sketched. Inset map (a) illustrates the major regional tectonic structures: AMT, front of the Appennine-Maghrebian thrust belt, separating the European domain to the north from the African carbonate platform to the south; CAW, Calabrian accretionary wedge (simplified from Gross et al., 2016; Polonia et al., 2016).

the fault line is ca. 5 mm/yr, but periods of accelerated slip have been reported in the past (Rasà et al., 1996). MCF also features similar fault behaviour, with the northern segment being seismogenic – but to a lesser degree - and the southern one creeping.

3. Recent seismotectonic activity: field evidence

After the M_L 3.41989 earthquake (Azzaro, 2004), in the following two decades SLF did not show any relevant activity, apart from the sluggish stable-sliding of its southern segment. In 2009, the northern segment ruptured seismically and creep events (i.e. accelerated

displacement episodes according to Wesson, 1988) occurred along the southern segment in 2016. Herein, we describe the effects produced by both the phenomena, which have been recognised by field surveys.

3.1. The 2009 earthquake

The seismicity started suddenly on May 13, 2009, when at 14:13 GMT an M_L 3.6 earthquake struck the lower eastern flank of Etna. As is common for shallow volcano-tectonic events of this magnitude, the shock had a felt area limited to some fifteen kilometres but produced noteworthy macroseismic effects in the epicentral area (details in
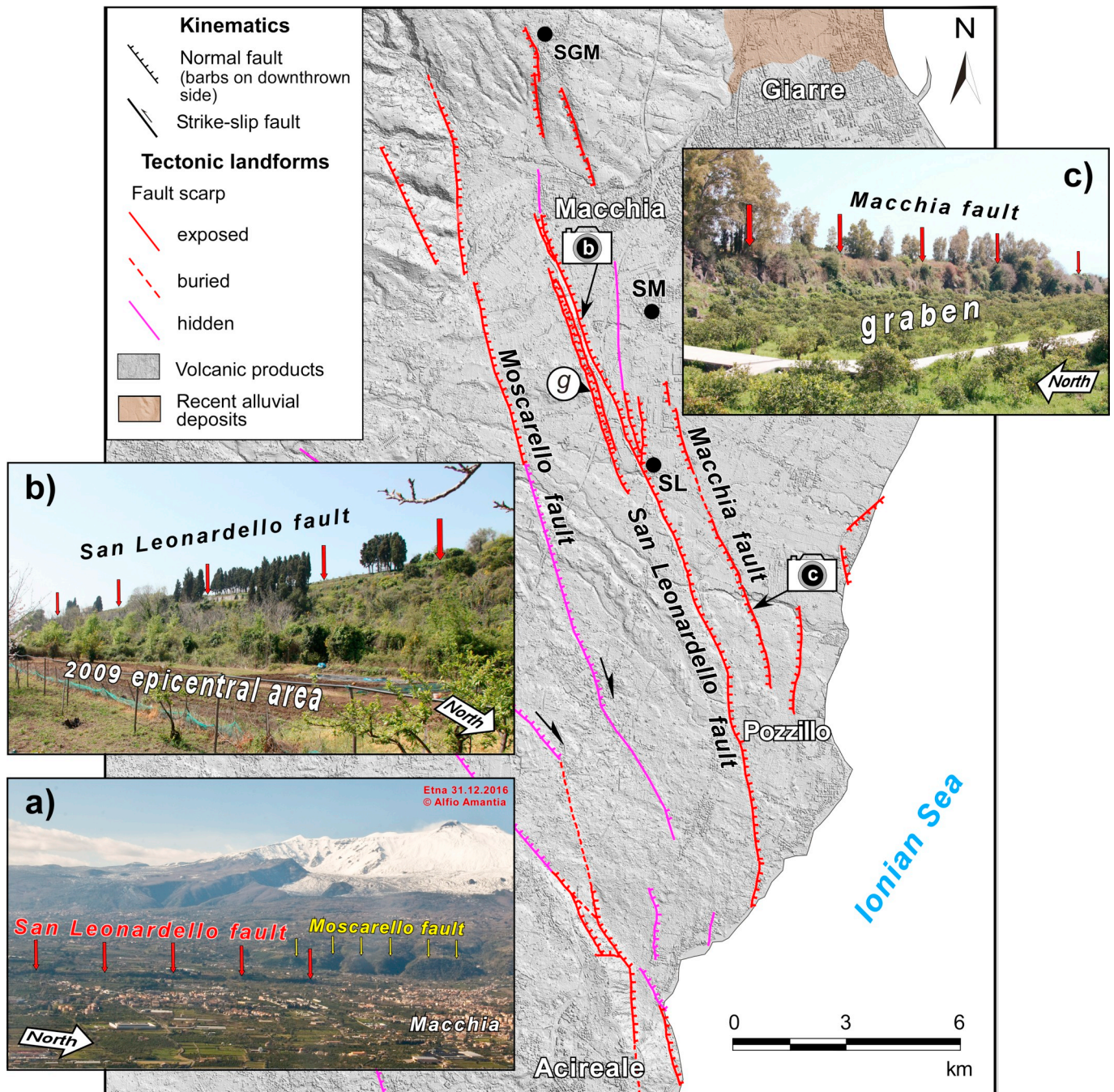
Fig. 2. Morphotectonic map of the studied sector of the Timpe fault system (from Azzaro et al., 2012). *g* indicates the graben west of the San Leonardello fault. Locality abbreviations: SGM, San Giovanni Montebello; SL, San Leonardello; SM, San Matteo. (a) Panoramic view (from east) of the central sector of the Timpe fault system; (b) View looking southwest along the northern segment of the San Leonardello fault; the scarp is ca. 35 m high; (c) Detail of the Macchia fault, bordering the graben to the east.

Azzaro et al., 2014). In brief, we observed that a narrow zone extending for 1.5 km in the hangingwall of SLF suffered diffuse but slight damage: reinforced concrete buildings had fine cracks in partition and infill walls but the partial collapse of a few old and more vulnerable rural houses occurred too (Fig. 4a, b). The maximum intensity was assessed as degree VI EMS, thus the 2009 earthquake should represent, from the historical-macroseismic point of view, a "minor" event in the seismic history of SLF (Fig. 3).

The 2009 earthquake also produced an evident surface faulting along the strike. We mapped a NNW-SSE-trending rupture zone developing for a length of 1.9 km on the hangingwall of SLF, and showing a kinematics characterised by a dextral oblique slip; the maximum

displacement (net slip) was measured at ~5 cm (Fig. 4c-e). Other seismogeological gravity effects such as small rockfalls and landslides were observed at the foot of the SLF escarpment. Finally, also from the tectonic point of view, the 2009 event seems smaller than the previous ones, which produced coseismic fracture systems extending up to 4 km in 1950, 3 km in 1989 and 2.5 km in 1920 (Azzaro, 1999).

3.2. The 2016 creep event

The long-period but steady aseismic slip along the southern segment of SLF accelerated abruptly on March 31, 2016 at the southern part of San Leonardello village, a locality where creep episodes have been
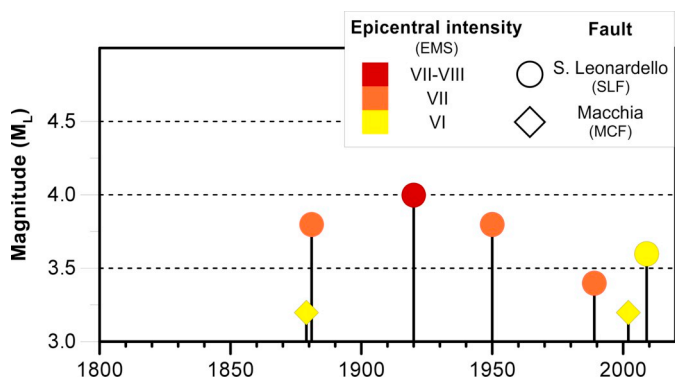
Fig. 3. Seismic history of the San Leonardello-Macchia fault system, reconstructed for major earthquakes above the damage threshold (data from Azzaro and D'Amico, 2019). Magnitude of events until 1950 are calculated according to the I-M relationship by Azzaro et al. (2011).

historically reported in the literature (Rasà et al., 1996; Gresta et al., 1997). We observed that a fracture system up to 1 km in length propagated rapidly (2–5 h) causing a right-lateral, oblique offset of the road SS 114 (Fig. 5), retaining walls and some buildings nearby. Soil cracks were aligned along a bearing of 160°, in a strip where past offsets are still visible.

In the next two months, we followed the aseismic slip propagating along the southern segment of SLF, which caused damage to buildings and other man-made structures located astride the ground-crack zone. Ruptures were characterised by similar kinematics, while offset gradually decayed to zero.

4. Seismological data

4.1. The 2009 seismic sequence

From May 13, 2009, after the M_L 3.6 mainshock, a significant seismic activity involving the lower eastern flank of Mt. Etna was being recorded by the permanent seismic monitoring system of the INGV-Osservatorio Etneo, which at the time consisted of thirty two 24-bit digital stations equipped with broadband (40 s) sensors, and other analogic short-period stations (Fig. 6a); in addition, with the aim of better constraining the event locations and improving the sequence study three temporary stations with broadband sensors were deployed close to the epicentral area.

In about a month, twenty-five earthquakes ($1.3 < M_L < 2.7$) were located in a range of 6–10 km from the mainshock epicentre (Alparone et al., 2015), whereas some forty micro-earthquakes were recorded only at 1–2 stations; several of these were also felt by people in the epicentral area of the mainshock. The hypocentral accuracy was improved by locating the events with a 3D velocity model (Patanè et al., 2006) and the software SIMULPS (Evans et al., 1994). Final hypocentres resulted with on average 0.05 s of residuals and 0.5 km of horizontal and vertical uncertainty (Table 1).

The event distribution in Fig. 6 clearly indicates that different fault strands were activated, producing a clustering pattern. In particular, the mainshock is located in the northern segment of SLF, at sea level; thereafter hypocentres migrated northward, likely also involving the tip of the nearest MF. Finally, in the period 10–14 June the seismic activity migrated some kilometres to the south.

4.2. Focal mechanism and source parameters of the 2009 mainshock

The focal solution of the M_L 3.6 event was calculated by using 28 polarities of the P-wave first motions recorded by the permanent seismic stations, according to the procedure described in Scarfi et al. (2013). Fig. 6b shows the kinematic parameters of the focal solution: in

particular, the NNW-SSE striking plane 2 is consistent with the tectonic setting and field evidence discussed before, and confirms a normal faulting with a dextral component of movement. The small magnitude of the events during the seismic sequence implies insufficient observational constraints to derive other focal mechanisms or other fault-plane solutions of previous earthquakes associated with this fault, are available in the literature.

The definition of source parameters of small earthquakes in a volcanic area is not an easy task, usually being computed from the displacement spectra of P- and S-waves. The seismic moment (M_0) controls the spectrum at low frequency, whereas the source dimension depends on the corner frequency (ω_c).

The waveform of the mainshock shows (Fig. 7), in the time domain, intermediate characteristics between a shallow Volcanic-Tectonic event (VT-B type, Wassermann, 2002) and the so-called hybrid type, i.e. the body waves are weakly emergent and a long-period component predominates in amplitude. This feature has already been observed at Etna in other shallow earthquakes (Patanè and Giampiccolo, 2004; Milana et al., 2008; Tusa and Langer, 2016), where the frequency domain analysis reveals a significant depletion in the high-frequency amplitude and a large spectral bump in the frequency band 0.1–1 Hz.

The procedure used here to calculate the earthquake displacement spectrum, is the following:

(i) rotation of the three ground components (V, N-S, E-W) to obtain P-radial and SH motions. These components were used to maximize the amplitude of the direct P-wave, and of the S component less contaminated by P motions. The azimuth and the incidence angle of rotation were extracted from the results of the earthquake location. Depending on S-P time, a P phase window extended for 256 or 512 samples was selected on the radial seismogram; for the S phase a window extended for 512 samples on the SH component was used. Stations located in the near-field, i.e. within 10 km from the epicentre, were discarded.

(ii) hanning window on P-radial and SH used to smooth the spectrum, before the determination of amplitude spectra by FFT.

(iii) deconvolution of the instrument amplitude response curve in the frequency domain; integration to obtain displacement spectra and deconvolution for the attenuation using the frequency dependent Q function proposed by Giampiccolo et al. (2007). The average attenuation laws $Q_P = 16 \cdot f^{0.8}$ and $Q_S = 32 \cdot f^{0.5}$ were used when no Q_P or Q_S data were available for the selected station.

The obtained spectra, 8 for P-radial and 9 for SH, were normalized to EMFS station distance to calculate the average spectrum for P-radial and SH and improve the resolution of the single estimates.

The obtained spectra are shown in Fig. 8, together with their average spectrum and theoretical model; by comparison, the spectra of seismic noise are also reported.

The average spectrum was inverted through linearization of the theoretical model based on the asymptotic fit of log-log displacement spectra (Boatwright, 1978, 1980) in order to obtain the spectral parameters, i.e. the low frequency level (Ω_0), the corner frequency (ω_c) and the high frequency fall-off beyond the corner frequency (γ). For both the components, ω_c which best fits with the model, is smaller than that generally calculated for earthquakes of such energy in Italy (Zollo et al., 2014) or in California (Abercrombie, 1995). The results obtained are in agreement with what has been observed by Milana et al. (2008) for other shallow earthquakes in the eastern flank of Etna. The seismic moment (M_0) was estimated by Keilis-Borok's (1959) relationship:

$$M_0 = 4\pi\rho V^3 R \frac{\Omega_0}{FU_{\theta,\varphi}}$$

where ρ is the density of the medium (2700 kg/m^3, Patanè and Giampiccolo, 2004; Giampiccolo et al., 2007), R is the hypocentral
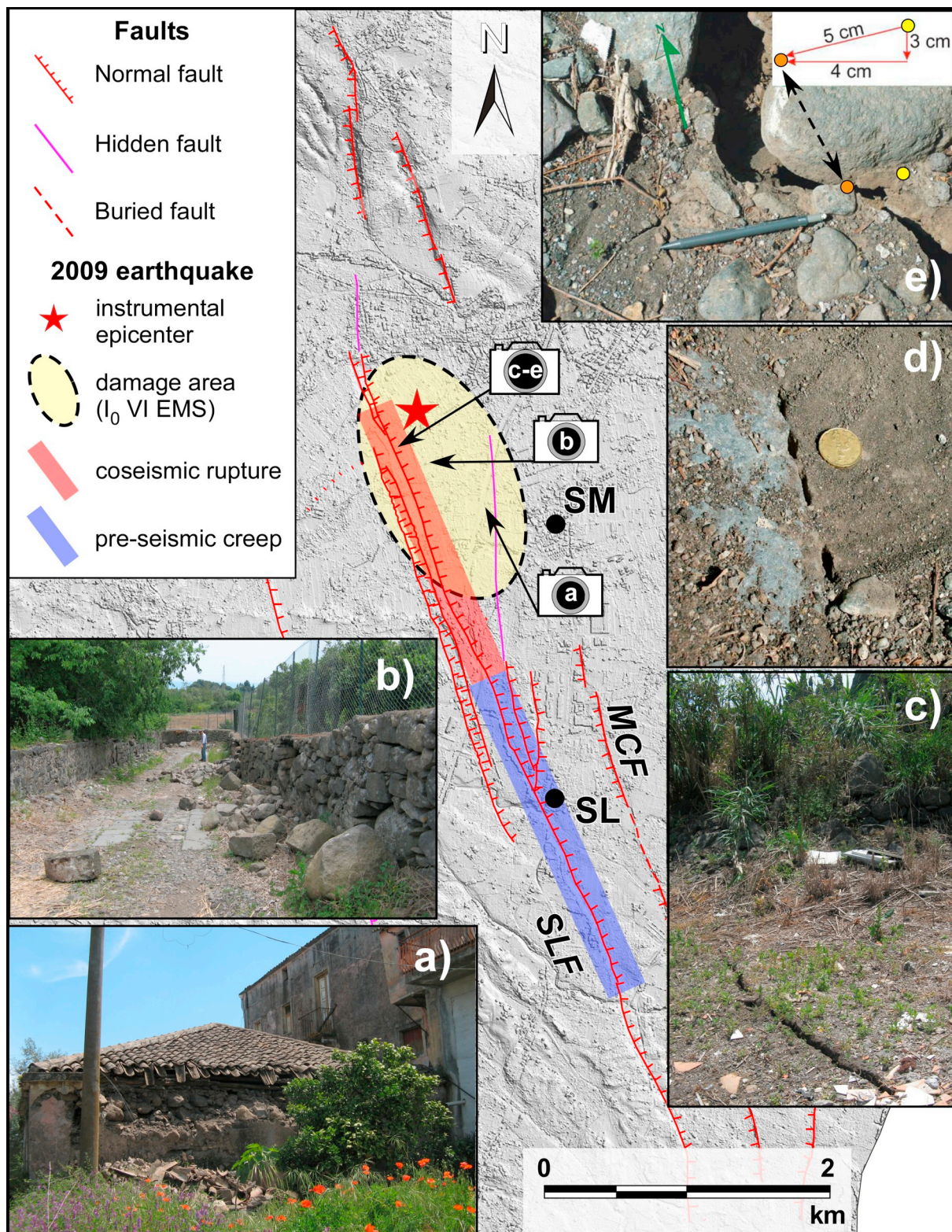
Fig. 4. Macroseismic effects and ground ruptures in the epicentral area of the 2009 earthquake. (a) Partial collapse of a rural building; (b) Damage and bending of a wall along a cart track; (c) Fracture system developed along bearings of 145°-150° in the hangingwall of the San Leonardello fault scarp (downthrown to the northeast); (d) Detail of the right-lateral component of movement (strike separation of 3 cm); (e) Scheme of displacement along the fracture line (3–7 cm in throw, 4 cm in heave).

distance (here assumed as the source-EMFS station distance), V is the wave velocity at the hypocentral depth (3.09 km/s for P-waves, 1.79 km/s for S-waves) of the 3D velocity model (Patanè et al., 2006), F is the free surface factor (assumed as 2), and $U_{\theta,\varphi}$ is the mean radiation pattern (0.4 for P waves, 0.25 for S waves, Giampiccolo et al., 2007). The source radius (r), the average displacement (u) and the stress drop ($\Delta\sigma$) were calculated following Madariaga (1979), by using the S-wave velocity V_S at the hypocentre depth and a shear module (µ) of 8.65 GPa.
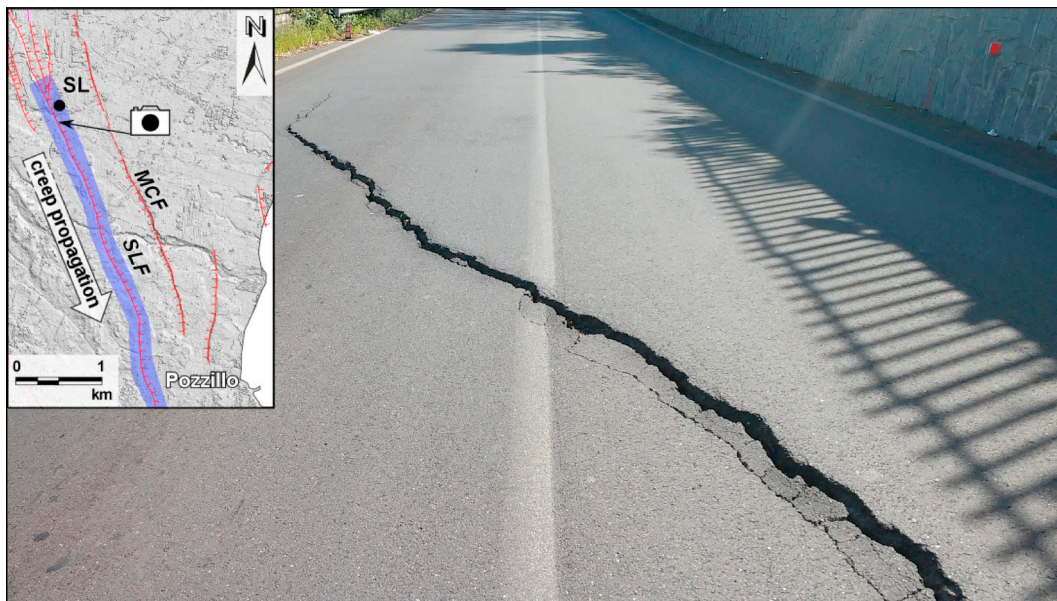
Fig. 5. Road SS 114, detail of the fracture line along the San Leonardello fault (view from north, lat. 37.68818, long. 15.17185). The right-lateral component of movement (strike separation of 2 cm) in addition to the vertical offset (4 cm in throw), is evident.

Results are shown in Table 2.

The values of the seismic moment obtained from the vertical and horizontal components were used to estimate the moment magnitude (M_W) through the Kanamori (1977) equation. We obtained M_W 4.0 for P waves and 3.9 for S waves, values larger than M_L 3.6 but similar to the M_W obtained by the tensor moment from Saraò et al. (2016), namely 3.9. The difference between M_L and M_W may be explained taking into account that in a Wood-Anderson sensor the frequency range below 0.8 Hz is filtered, causing, in the case of earthquakes with a predominant content of low-frequency, an underestimation of the maximum amplitude of the horizontal component and hence of the local magnitude value (Milana et al., 2008). The scaling relationship between M_0 and ω_c obtained by Giampiccolo et al. (2007) for high frequency earthquakes at Etna, produces for an M_W 4.0 event a corner frequency of ca. 2.0°, a very different value from the one calculated for the May 13, 2009 mainshock. The small values of ω_c obtained in our analysis, imply a larger fault radius and smaller displacement than expected for similar high frequency earthquakes.

For the same reason, the values of the stress drop ($\Delta\sigma$) indicated in Table 1, are lower than the ones generally obtained for events with the same magnitude in purely tectonic domains, and can be explained by the shallowness of the earthquake (Sumy et al., 2017). Moreover, values of stress drop less than 2 MPa are reported in areas characterised by the occurrence of slow events or low frequency earthquakes (Brodsky and Mori, 2007), as observed also by Palano (2016) and Bruno et al. (2017) in the eastern flank of Etna.

4.3. The 2016 seismic activity

In 2016, the beginning of creep activity at the end of March did not trigger seismicity along SLF; only two earthquakes of ca. M_L 2 were located a few kilometres to the south. Later, between 10 and 29 April, eight earthquakes ($0.8 < M_L < 2.6$) affected the same epicentral area of the 2009 sequence, again along the northern segment of the fault (Fig. 6, Table 1). Event location resulted in very shallow hypocentres for most of them, according to the recorded waveforms characterised by emerging arrivals and low-frequency spectral contents, as observed for the 2009 sequence.

5. Ground deformation

5.1. The 2009 seismic period

In summer 2008, a local GNSS array was installed along the northern segment of SLF in order to improve the resolution of the Etna GPS permanent network locally. The first campaign was carried out in November 2008 and a second set of measurements repeated in April 2009, about one month prior to the onset of the seismic activity described previously (chap. 4.1); the third geodetic survey was then measured on May 20, one week after the M_W 4.0 mainshock (Fig. 9).

As usual, the local GNSS array data (Bonforte et al., 2016a, 2016b, here available in Supplementary Material) were processed using the same procedures adopted for the periodic monitoring surveys (Bonforte et al., 2008). In brief, data acquired across SLF were processed in a wider frame, together with the Etna permanent GNSS network data, by using IGS final precise ephemerides and accurate antenna calibration models in order to achieve the maximum precision in the final positioning of the stations. In this way, as is usually done for other surveys at Etna, the stations across SLF are constrained in a more complete frame, resulting in a total of 42 stations with 1953 baselines for the April survey, and 34 stations with 616 baselines for the May campaign. This procedure allows precise constraints to be applied for the final positioning of each station, thanks to the high degree of redundancy and connections between points (each station is connected to the others by 20 or more measured baselines) when performing the final network adjustments. The final results of the two surveys (station coordinates and associated errors resulting from the network adjustments) are reported in Table 3.

The main features are: i) the vertical displacements are prevailing with respect the horizontal ones, and ii) the maximum subsidence, up to ca. 6 cm (differential between hangingwall and footwall), is measured close to the epicentral area of the M_W 4.0 mainshock. Unfortunately, the occurrence of near-field effects determined a dispersion in the strike of the horizontal displacement vectors, making it difficult to reconstruct the fault kinematics. A more complete picture of the overall deformation accommodated by the fault emerges from the analysis of InSAR data. To this end, we used different satellite data to investigate fault dynamics in the short- and mid-term.

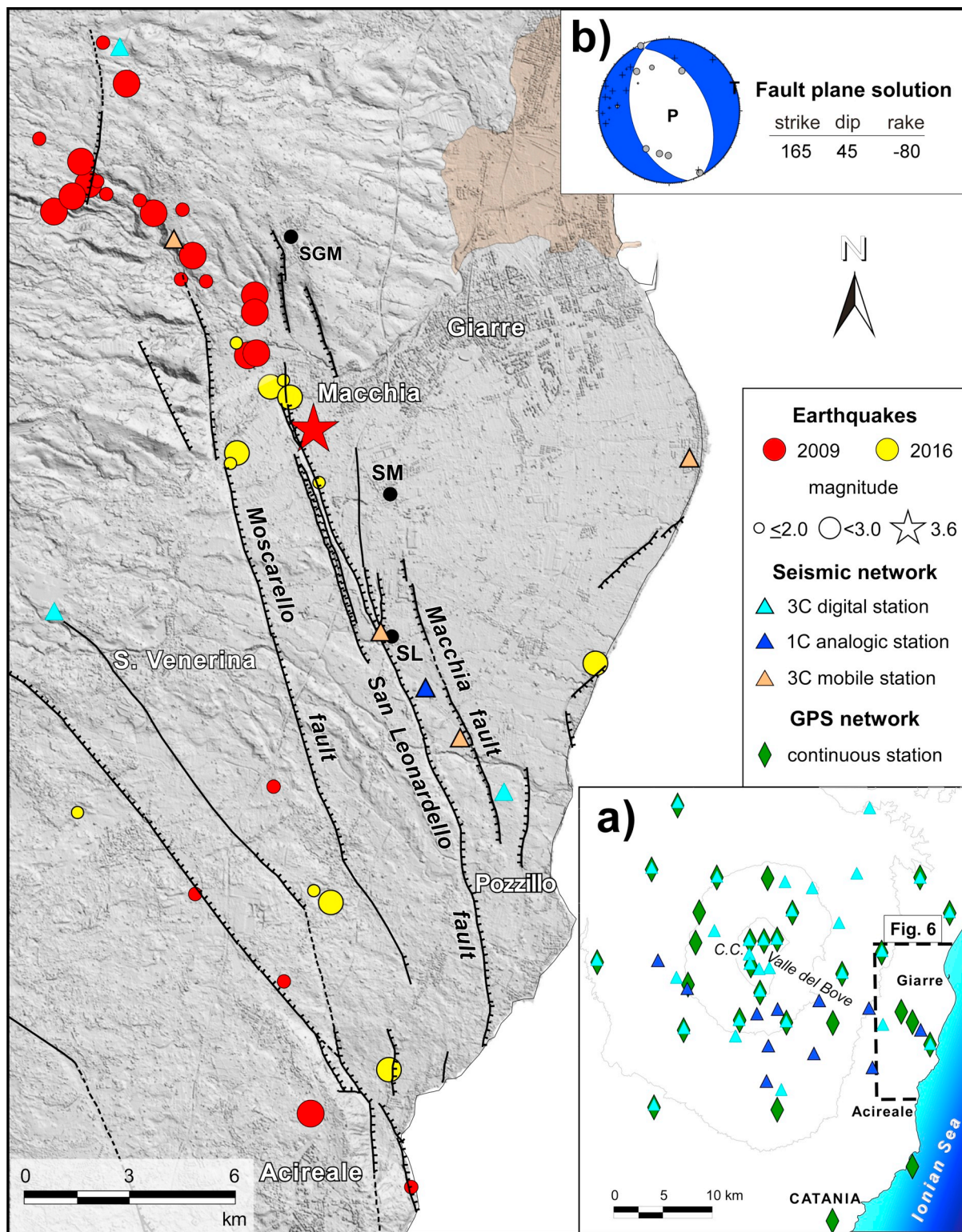Fig. 10a shows the interferogram resulting from ENVISAT images

Fig. 6. Epicentral map of the earthquakes listed in Table 1, located using a 3D velocity model with SIMULPS algorithm. (a) Distribution of the seismic and GNSS stations in the Etna region; (b) Fault plane solution of the M_L 3.6, 2009 mainshock.

acquired in ascending orbits during a time-span of 35 days in between the mainshock on May 13: it is clearly evident that the maximum deformation corresponds to the epicentral area of the M_W 4.0 earthquake (cfr. Fig. 4), with an offset of −6 cm defining a displaced zone that extends for 1.5 km along the SLF hangingwall (section E-W 1 in Fig. 10b).

This pattern confirms that the observed deformation is indeed

coseismic and well-confined along the strike since there is no apparent displacement as far as section E-W 2 to the south; here, the creeping section of the fault displays a minor offset that progressively decays towards the southern termination (section E-W 3).

The same deformation pattern emerges from the analysis of ALOS satellite data acquired in the period 2007–2010. A total of 17 ascending images have been processed by means of STaMPS package (Hooper,

Table 1
Main parameters of the earthquakes reported in Fig. 6.

| Date	Origin time	Lat	Long	Depth (km b.s.l.)	M_L	RMS	Err. X	Err. Y	Err. Z
08/05/2009	20.11.06	37.741333	15.13250	0.19	1.3	0.08	0.069	0.064	0.108
09/05/2009	11.53.24	37.740500	15.13750	0.52	1.5	0.11	0.079	0.081	0.110
13/05/2009	14.13.46	37.713333	15.16183	0.08	3.6	0.06	0.052	0.043	0.254
15/05/2009	03.59.25	37.742833	15.13116	0.47	1.8	0.12	0.069	0.060	0.094
15/05/2009	03.59.40	37.739000	15.13933	0.00	2.0	0.08	0.096	0.057	0.137
15/05/2009	11.42.32	37.742333	15.13000	0.70	2.3	0.12	0.062	0.050	0.098
16/05/2009	11.19.09	37.721833	15.15233	−0.01	2.4	0.10	0.082	0.056	0.134
16/05/2009	11.57.27	37.722167	15.15350	0.11	2.1	0.08	0.068	0.049	0.130
17/05/2009	08.02.52	37.726667	15.15283	0.15	2.2	0.09	0.079	0.054	0.101
17/05/2009	09.03.50	37.672500	15.15567	0.30	1.9	0.04	0.124	0.305	1.095
18/05/2009	14.12.45	37.729000	15.15317	−0.14	2.4	0.06	0.067	0.052	0.105
18/05/2009	14.55.05	37.745000	15.12900	0.30	2.2	0.15	0.047	0.047	0.075
21/05/2009	09.00.22	37.739333	15.14367	0.00	1.7	0.11	0.200	0.186	0.135
24/05/2009	09.46.37	37.753833	15.13567	−0.10	2.2	0.14	0.044	0.036	0.040
24/05/2009	22.05.06	37.758667	15.13233	0.04	1.6	0.20	0.160	0.056	0.340
27/05/2009	19.37.03	37.739667	15.12533	1.34	2.7	0.12	0.079	0.052	0.099
28/05/2009	06.50.00	37.741167	15.12767	0.37	2.3	0.10	0.073	0.052	0.109
05/06/2009	23.53.31	37.747667	15.12283	0.51	1.2	0.07	0.084	0.077	0.117
10/06/2009	01.51.14	37.660167	15.14417	1.65	1.5	0.08	0.089	0.160	0.218
14/06/2009	00.26.08	37.650000	15.15700	0.51	1.7	0.11	0.077	0.146	0.126
14/06/2009	21.47.43	37.635000	15.16067	−0.25	2.2	0.19	0.088	0.177	0.134
18/06/2009	22.52.38	37.730667	15.14233	−0.01	1.4	0.12	0.164	0.059	0.202
19/06/2009	16.15.58	37.730333	15.14600	0.00	1.3	0.08	0.119	0.068	0.272
19/06/2009	16.26.27	37.733333	15.14417	0.15	2.4	0.10	0.082	0.050	0.125
31/03/2016	01.40.34	37.658333	15.16400	0.00	2.2	0.10	0.131	0.369	0.497
03/04/2016	06.36.03	37.639000	15.17250	0.01	2.1	0.32	0.124	0.206	0.227
04/04/2016	21.41.37	37.686000	15.20250	0.00	2.2	0.19	0.134	0.099	0.175
10/04/2016	03.50.06	37.709500	15.14950	0.19	1.6	0.09	0.073	0.046	0.178
14/04/2016	12.58.29	37.723500	15.15067	0.00	1.8	0.09	0.085	0.044	0.170
14/04/2016	23.56.57	37.717000	15.15800	0.00	2.1	0.16	0.065	0.049	0.142
16/04/2016	05.25.24	37.747667	15.12650	3.43	0.8	0.07	0.222	0.145	0.172
26/04/2016	23.56.02	37.718333	15.15550	1.06	2.6	0.17	0.062	0.064	0.140
27/04/2016	01.20.13	37.719167	15.15717	0.02	1.6	0.10	0.067	0.047	0.125
27/04/2016	17.49.06	37.710833	15.15033	2.77	2.3	0.14	0.049	0.046	0.096
27/04/2016	17.51.02	37.669167	15.12783	9.69	1.4	0.20	0.377	0.469	0.318
29/04/2016	00.15.52	37.659833	15.16183	2.88	1.5	0.15	0.082	0.092	0.109
29/04/2016	12.22.22	37.707167	15.16250	8.59	1.0	0.03	0.387	0.376	0.481
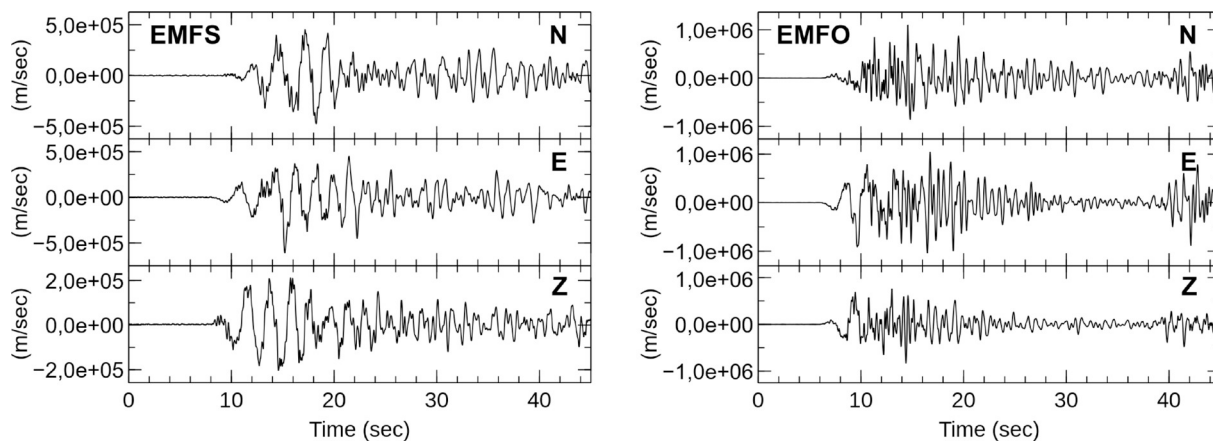
Fig. 7. Seismograms of the May 13, 2009 earthquake as recorded at EMFS and EMFO stations, respectively, 14.1 and 6.6 km far from the epicentre.

2008) in order to build the time series of LOS velocity for each coherent pixel. The resulting map, shown in Fig. 11a, depicts the mean velocities of the ground deformation detected in this part of the volcano over four years, a time-span we consider representative of the fault behaviour in the mid-term (that includes both continuous deformation cumulating on the creeping segment of the fault, and episodic accelerations occasionally displacing the locked section): the two blocks moving at different velocities are clearly separated by SLF, whose fault trace extends as far as the coast line to the south. The only part where the abrupt velocity change is not appreciable is marked by white arrows in Fig. 11a, corresponding to the zone just to the north of section E-W 2 in

Fig. 10, in agreement with the interferogram. The area where the velocity difference is most pronounced coincides with the maximum displacement area detected by the short-term ENVISAT interferogram in Fig. 10. Here, the ground LOS velocity profile (AA', Fig. 11b) shows the abrupt jump well, corresponding to SLF; it decouples the western block characterised by a mean velocity near to 0 mm/y, from the eastern sector where the ground moves away from the satellite (which means eastwards and/or downwards) at a rate of ca. 20–30 mm/y. These are mean velocities, calculated linearly over the entire 2007–2010 period.

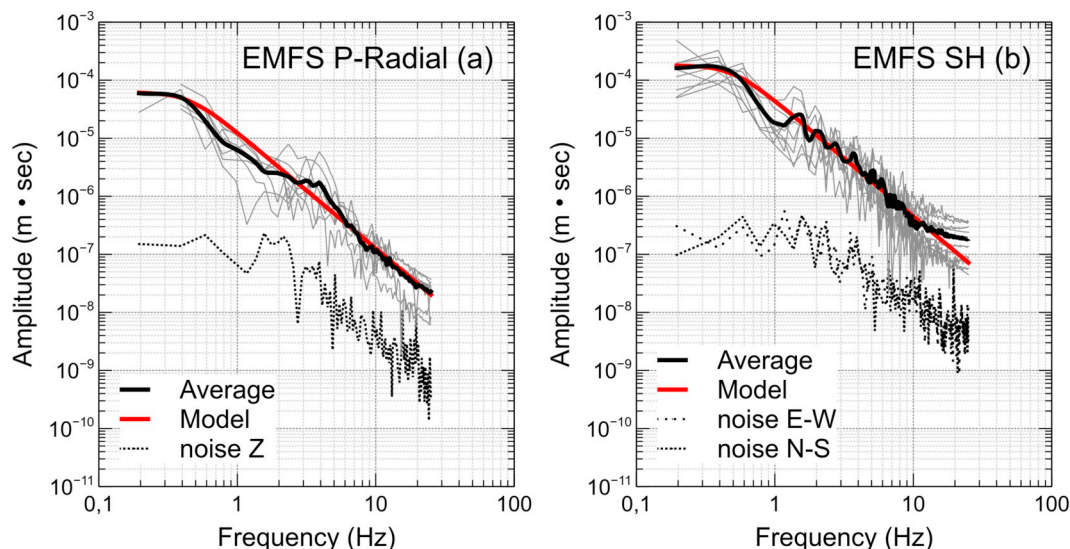In order to observe the progression of deformation over time, we

Fig. 8. Displacement spectra for P-radial (a) and SH (b) components. Thick black lines: average spectra; red lines: theoretical model; dotted lines: spectra of noise. (For interpretation of the references to colour in this figure legend, the reader is referred to the web version of this article.)

Table 2
Spectral parameters and related seismic source data calculated for the May 13, 2009 mainshock.

	Ω_0 (m·sec)	ω_c	γ	M_0 (N·m)	M_W	r (m)	u (cm)	$\Delta\sigma$ (Mpa)
P-radial	$6.22 \cdot 10{-}5$	0.45°	2.0	$1.10 \cdot 1015$	4.0	1273	2.79	0.233
SH	$1.80 \cdot 10{-}4$	0.50°	2.0	$9.88 \cdot 1014$	3.9	1298	2.16	0.198

Ω_0: low frequency level; ω_c: corner frequency; γ: high frequency fall-off; M_0: seismic moment; M_W: moment magnitude; r: fault radius; u: average displacement; $\Delta\sigma$: stress drop.

extracted the differential time-series of LOS displacements calculated for two pixels lying on the hangingwall and footwall of the fault, across the same section discussed before. In Fig. 11c a general constant movement of the fault is evident, with the hangingwall moving away from the satellite more than the footwall, accumulating about 10 mm from 2007 to 2009 until the May 13, 2009 earthquake, which produces a sudden dislocation of about 55 mm between the two pixels. This value is in good agreement with the deformation detected by ENVISAT data in Fig. 10. The InSAR time series in Fig. 11c also indicates that, in the months following the seismic event, the displacement continues at about the same rate as before.

5.2. The 2016 creep event

In 2016, no GNSS data is available for the area close to the fault and during the short time-window spanning the creep event (like in 2009) but we took advantage of the new constellation of Sentinel-1A SAR satellites, characterised by a significantly shorter revisiting time (12 days, 6 days using ascending and descending orbits) with respect to the previous Envisat sensor (35 days in the same orbit/geometry). This adds a higher temporal resolution to the already very high spatial detail of the ground deformation pattern obtained by the spatial remote sensing DInSAR technique. During the period March–April 2016, we were able to detect a very interesting creep event and analyse its evolution along the fault prior to the seismic swarm. We exploited the images acquired on March 19 and 31, April 12 and May 06 in ascending orbit, and on March 25, April 06 and 30 in descending orbit, and combined them to produce six interferograms (three for the ascending and three for the descending view).

Looking at the ascending interferograms, the March 19–31 pair highlights a first local LOS displacement episode (E1) of about 2 cm in

the central part of the SLF (Fig. 12a). The next image, acquired on April 12, combined with the March 31 one (Fig. 12b), reveals a new LOS displacement of the same order of magnitude but affecting an adjacent segment of the fault, just south of the previous one (E2). A longer-period interferogram (March 19–May 06 ascending pair, Fig. 12c) displays the overall displacement occurring during the entire deformation episode, affecting a 2.5 km long section of SLF. The fault movement progressively propagated from the northern tip of the creep segment (cfr. Fig. 1) (between March 19 and 31) towards the south (between March 31 and April 12) in about one month, also showing a minor LOS deformation along the southernmost section of the antithetic MCF in the second half of April (E3).

The descending pair acquired in the time-span March 25 – April 06 (Fig. 12d) shows the deformation of the whole central segment of SLF similarly to the cumulative March 31 – April 12 ascending pair (Fig. 12b). The next descending pair, April 6–30 (Fig. 12e), "catches" the deformation occurring to the south along the antithetic MCF better. This is due to the west dipping geometry of the fault plane, the vertical (downwards) and horizontal (westwards) components of motion producing opposite LOS variations in the ascending view, while they cumulate in the descending geometry (see Fig. 3 in Bonforte et al., 2011). The cumulative deformation related with the 2016 creep event can be very clearly observed in the descending pair covering the March 25 – April 30 time-span (Fig. 12f), highlighting the interaction of the two faults.

By considering the alternate dates of both ascending and descending passes (timeline in Fig. 12), it is possible to apply a further temporal constraint on the dynamics of the central part of SLF, allowing us to assess that the entire creep event started after March 25 and ended before April 6. Moreover, if we combine this information with the detail provided by the ascending pairs, we can follow the evolution of the phenomenon, defining the timing of the first episode (E1) between March 25 and 31, and that of the second one (E2) between March 31 and April 6. Finally, the third episode affecting MCF (E3) occurred after April 12 and ended before the end of the month.

For all the interferograms (both ascending and descending), we plotted the LOS ground displacements observed along three different profiles crossing different portions of SLF and MCF. The resulting cross-sections of the ground motion clearly show the abrupt displacement related to the two faults, producing the subsidence of the hangingwall as well as a slight uplift of the footwall. Due to the opposite looking geometries, LOS displacements of the footwall of the SLF during E1 and
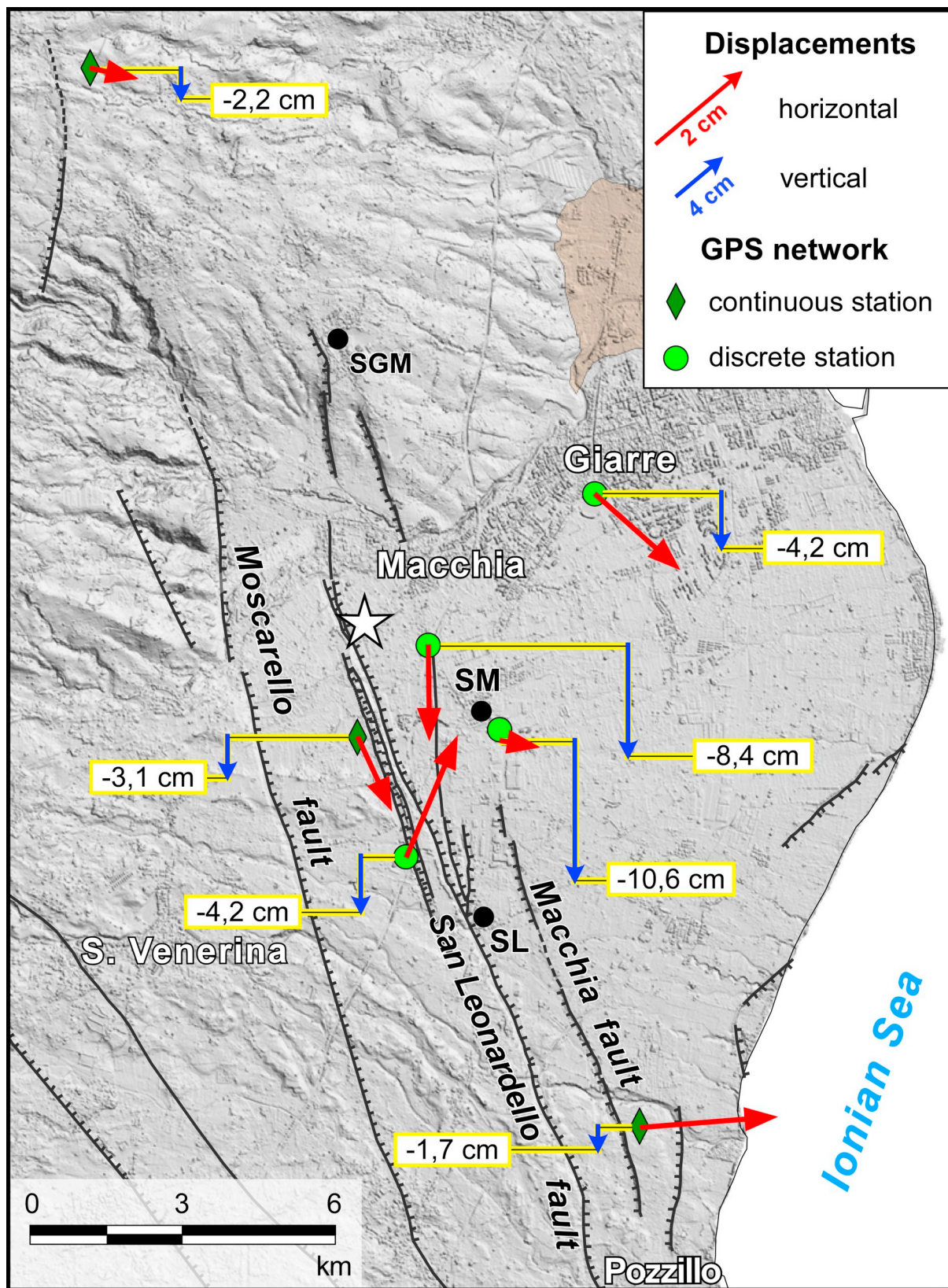
Fig. 9. Ground displacements measured by the continuous and discrete GNSS stations in the time-span Apr 7- May 20, 2009. Errors: horizontal 0.22 cm, vertical 0.36 cm. The star indicates the epicentre of the May 13, 2009 mainshock.

E2 episodes are smaller on descending geometry (Profiles AA' and BB' in Fig. 12, respectively). This difference reveals a significant horizontal (i.e. westwards) component of motion on the western side of the fault.

On the hangingwall, the eastern component of movement produces a positive LOS displacement (moving away from the sensor) for the ascending view, and an opposite effect (approaching the sensor) for the

Table 3

Final adjusted coordinates and associated errors resulting by each survey processing (m), in WGS84, UTM projection – zone 33 N, and comparison for station displacements.

Point name	Easting	E error	Northing	N error	Height	h error
April 2009 survey						
EBAG	514,170.256	0.001	4,172,804.410	0.001	280.112	0.001
ECDV	514,606.505	0.001	4,171,845.643	0.001	245.104	0.002
EGIA	516,241.855	0.001	4,174,962.829	0.001	141.741	0.001
EMCH	514,797.641	0.001	4,173,683.724	0.001	223.577	0.002
EPOZ	516,626.612	0.001	4,169,432.566	0.001	109.072	0.001
ETRP	515,411.131	0.001	4,172,853.139	0.001	205.322	0.002
May 2009 survey						
EBAG	514,170.262	0.002	4,172,804.397	0.002	280.081	0.002
ECDV	514,606.514	0.002	4,171,845.664	0.002	245.062	0.003
EGIA	516,241.870	0.002	4,174,962.816	0.002	141.699	0.002
EMCH	514,797.641	0.002	4,173,683.707	0.002	223.493	0.003
EPOZ	516,626.636	0.002	4,169,432.568	0.002	109.055	0.002
ETRP	515,411.138	0.002	4,172,853.138	0.002	205.216	0.003
Coordinates comparison						
EBAG	0.006	0.002	−0.013	0.002	−0.031	0.002
ECDV	0.009	0.002	0.021	0.002	−0.042	0.004
EGIA	0.015	0.002	−0.013	0.002	−0.042	0.002
EMCH	0.000	0.002	−0.017	0.002	−0.084	0.004
EPOZ	0.024	0.002	0.002	0.002	−0.017	0.002
ETRP	0.007	0.002	−0.001	0.002	−0.106	0.004

descending one.

Conversely, during the E3 episode occurring on the west-dipping MCF, the rebound of the footwall, with eastward component of motion, produces positive (approaching) LOS displacement on the descending view and an opposite effect on the ascending one, while the very similar values of LOS displacement of the hangingwall reveal a mainly vertical component (subsidence) of motion (Profile CC' in Fig. 12).

6. Discussion

In the following, we compare and integrate results coming from the different investigation approaches into a conceptual model. Field data (macroseismic and tectonic surveys) provide entirely consistent evidence with the instrumental seismological features, as well as the overall deformation picture measured by GNSS and InSAR techniques. Due to the shallowness of the source of deformation and the non-elastic behaviour of the medium revealed by GNSS and InSAR data in the near-field, an analytical inversion of the geodetic datasets using elastic models cannot be performed. Conversely, we take advantage of the complexity and completeness of field data, seismological analyses and geodetic observations to exploit the complementarity of information provided by distinct and independent approaches. In fact, each approach reveals and highlights different aspects of the fault activity occurring in 2009 and 2016 and, taken together, allow understanding the significance of the type of deformation (coseismic displacement and creep) in terms of fault behaviour. To this end, we proceed by zooming out from the scale of the seismic asperity (source parameters) to the distribution of deformation (InSAR data) along the strike.

The radius (r) of the seismic source of the 2009 mainshock, is of ca. 1.3 km (see Table 2). Considering the depth of the hypocentre (0.08 km b.s.l.) and the topographic elevation (ca. 0.2 km a.s.l.), the intersection of the focal volume with the topographic surface measures about 2.5 km (Fig. 13a, black line). This value is compatible with the length of the coseismic rupture measured in the field, reaching 1.9 km (blue line in Fig. 13a). On the other hand, the extension of the most prominent deformation area detected by the ENVISAT InSAR data (the red area in Fig. 10a), is ca. 2.8 km (green line in Fig. 13a). Regarding the average displacement (u), the value obtained from the seismic source parameters is rather small, in the range 2.2–2.8 cm (Table 2), consistent
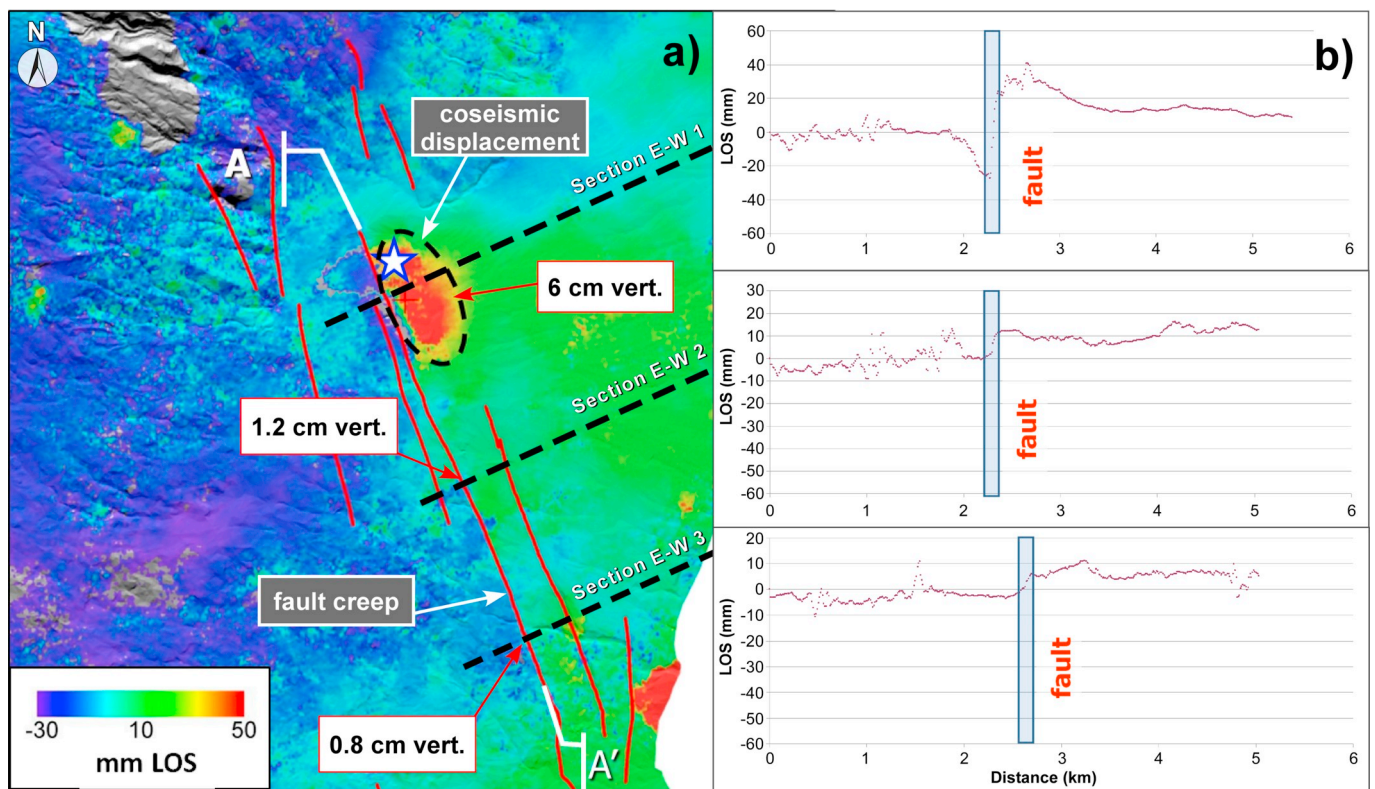

Fig. 10. (a) Pattern of deformation obtained by ENVISAT data: time-span Apr 15-May 20, 2009, ascending geometry. Star and dashed ellipse represent the epicentre and maximum effect area of the M_w 4.0 May 13, 2009 earthquake; (b) Cross-sections showing the variation of the LOS offset along SLF. Increasing LOS distance, for ascending view, means that the ground is moving downwards and/or eastwards.
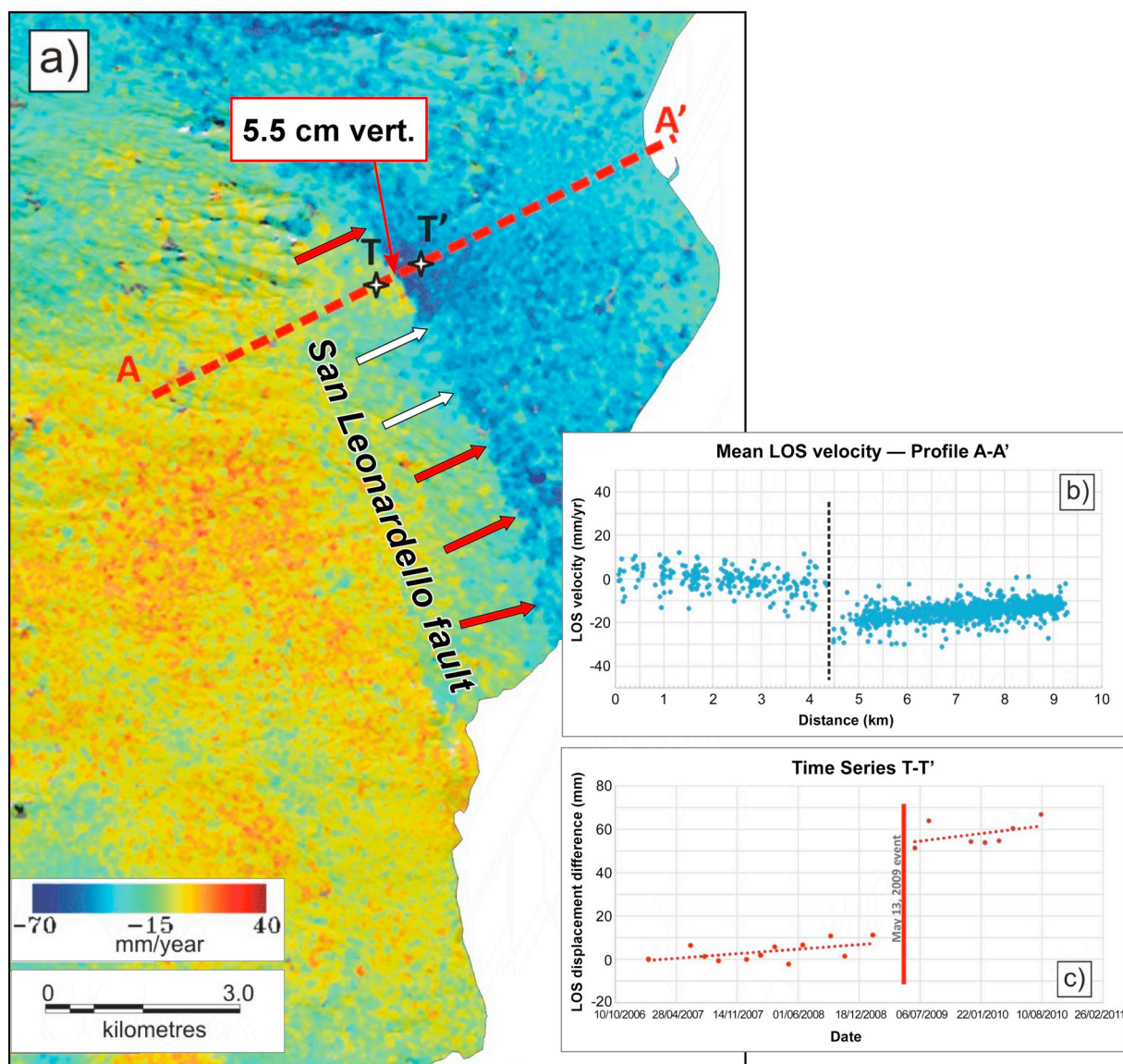
Fig. 11. (a) Mean LOS velocity obtained by A-DInSAR analysis of ALOS data: time-span 2007–10, ascending geometry, processed by Persistent Scatterers Technique. Red arrows mark the SLF trace, in white the locked section of the fault; (b) Mean LOS ground velocities measured along the A-A' profile crossing the fault and the epicentral area of the May 13, 2009 earthquake; (c) Differential time-series of LOS displacement between T and T' pixels, showing the 2009 coseismic offset and the continuous fault creep. (For interpretation of the references to colour in this figure legend, the reader is referred to the web version of this article.)

with the average displacement of 2.7 cm calculated from the LOS profiles throughout the maximum coseismic deformation area (yellow in Fig. 13b). As for the maximum net slip, we note a close similarity between the value observed in the field along the surface rupture, and the one calculated by InSAR data, both in the range 5–5.5 cm.

Looking at the fault scale, Fig. 13b highlights the spatial relationship between the 2009 seismic source and the fault displacements detected by DInSAR measurements in the 35-day interval (for the location of profile A-A', see Fig. 10a). We note that the maximum deformation corresponds to the focal volume of the M_W 4.02009 earthquake, well-represented by the damaged area identified by the macroseismic survey (see Fig. 4), while displacement progressively decreases southward until zero at a distance of 3.3 km. From here southwards, we observe an abrupt change in the deformation pattern, with a rather uniform displacement - around 1 cm between the footwall and hangingwall - as far the southernmost termination of the fault.

While profile A-A' in Fig. 13b fixes the fault dynamics in the short-term (15 Apr − 20 May 2009), highlighting how the displacement is differently distributed along the strike, the mid-term (2007–2010) ALOS velocity/time series (Fig. 11b, c) confirm that the offset produced by the 2009 earthquake remains the same (5.5 cm), whereas the signature colour of a continuing deformation marks the fault line to the south more clearly (Fig. 11a). As a result, these data corroborate the recent and historical field evidence of surface faulting, i.e. the segment to the north is locked and releases episodically the cumulated elastic deformation while creeping to the south contributes to load the structure. In this framework, the most recent creep episode in 2016 does not add further evidence but clarifies the mode of stable-sliding, characterised by the migration of deformation southwards (Fig. 12a-b), according to the field observations (see Fig. 5), but maintaining the offset constant.

As a last point, we have sought to unscramble the overall effect of short-term dynamics discussed above in terms of long-term fault activity, focusing on an indicator commonly considered in extensional features such as the morphological offset (see for example Lehner and Urai, 2000). By using a high resolution 1 m-DEM (Gwinner et al., 2006),
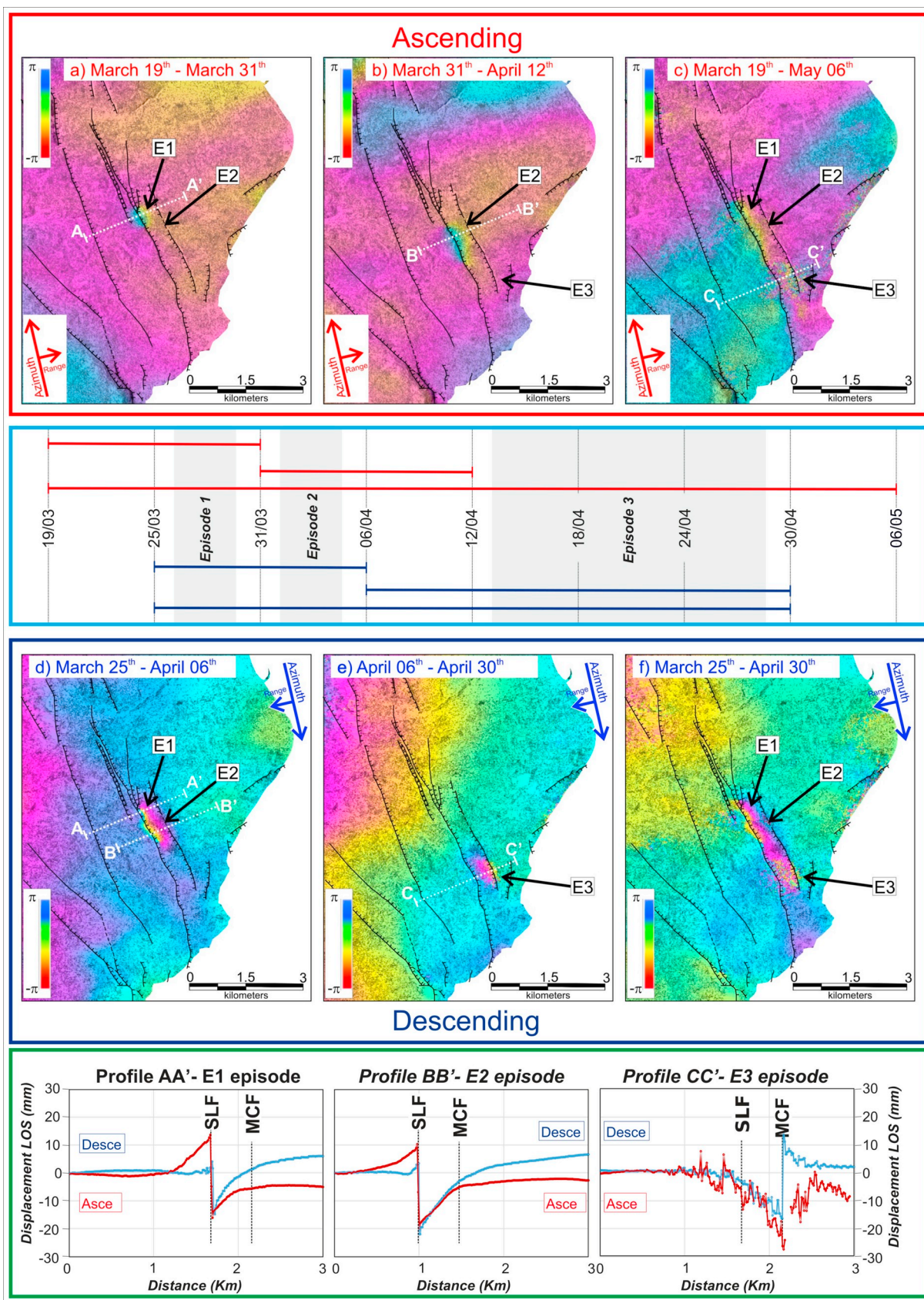
Fig. 12. Summary of the InSAR data analysed to characterize the 2016 creep event. Ascending (a-c) and descending (d-f) pairs showing the spatio-temporal evolution of the 2016 creep event; in the middle, the sketch of the time-windows analysed for defining the timing of the three creep episodes (E1, E2, E3). Bottom: profiles orthogonal to the faults, showing the cumulative LOS displacement produced during each creep episode.
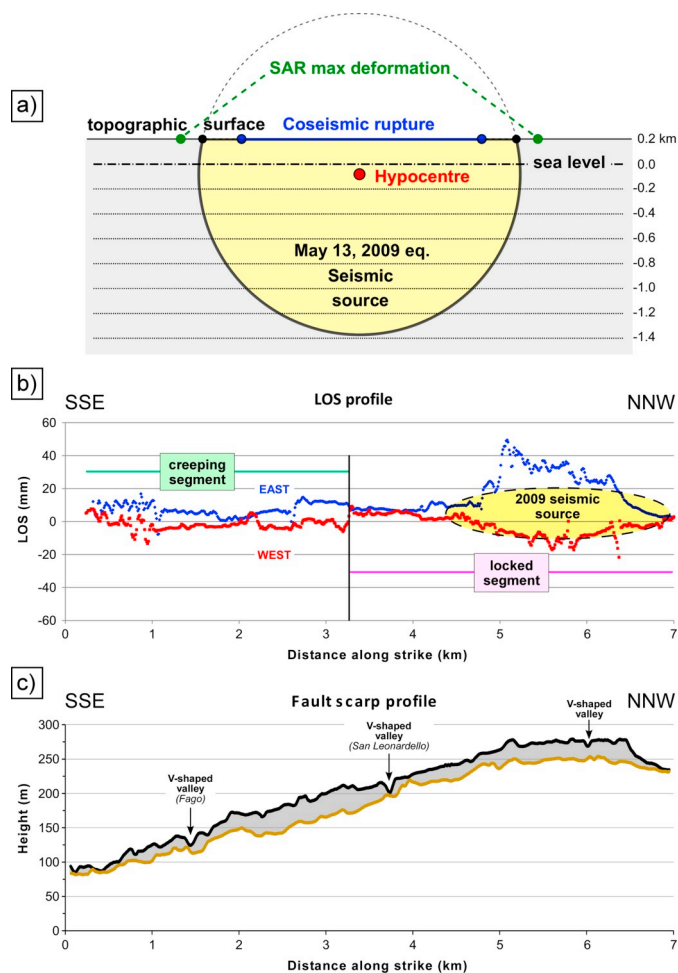
Fig. 13. (a) Seismological model of the seismic source obtained by the spectral parameters of the M_W 4.0, 2009 earthquake. Earthquake hypocentre located at the depth of 0.08 km b.s.l., with radius of 1.3 km; the intersection between the circular source and the topographic surface is 2.5 km long, a value consistent with the length of the coseismic surface rupture (1.9 km) and the max deformation area measured by SAR (2.8 km). (b) Distribution of the LOS displacements measured on the profile A-A' in Fig. 10a, referring to the footwall (in blue) and hangingwall (in red) of SLF, obtained by ENVISAT images (timespan 15 Apr-20 May 2009, ascending geometry). (c) Variation of the fault scarp height along strike, obtained from a 1 m-resolution DEM; the black and brown lines represent the topographic profiles running 30 m apart from the fault trace and parallel to it, along the footwall and hangingwall, respectively. Note the different tapering of the offset at the fault tips and the presence of small V-shaped valleys due to fluvial incision cutting downward into the footwall. (For interpretation of the references to colour in this figure legend, the reader is referred to the web version of this article.)

we traced two topographic profiles parallel to the fault, 40 m apart from the surface trace, along the footwall and hangingwall of SLF represented, respectively, as black and brown lines in Fig. 14c. Topography data have been averaged by applying a 50-sample moving window in order to smooth the noise due to the original high resolution of the DEM (10 cm in height), very sensitive to anthropic or micro-topographic features; in this way we obtained, with a reasonable approximation, the variability of the down-dip fault height along the strike. We note that the offset is fairly regular and homogeneously distributed but the taper at the fault tips is very different, very sharp to the north but progressively smoothed to the south. This trend very clearly mimics the pattern of short-term displacements shown in Fig. 13b. Moreover, apart from a series of residual local disturbances, we also observe some river incisions, mainly cutting downward into the footwall (black line in Fig. 13c); conversely, note that the same

evidence is barely visible in the hangingwall (brown line). This feature confirms the intense tectonic uplift due to the fault activity in the long-term.

Moving on to the conceptual model of SLF, Fig. 14a shows the summary of results discussed above; we wish to highlight now some aspects concerning the seismogenic potential of the fault. The first point derives from the characteristics of the earthquake surface faulting. We note that during the historical events shown in Fig. 3 (Azzaro, 1999), i) no coseismic faulting extended into the creeping section (in blue in Fig. 14a), ii) the ruptures reached maximum lengths up to 4 km and iii) they affected only the sector of the fault characterised by a well-defined scarp (in grey in Fig. 14a).

Looking at the distributions of the 2009 aftershocks (orange dots in Fig. 14a), we notice that a part of them ruptured beyond the fault tip, in a sector where the tectonic activity has not yet produced a clear morphological evidence (in white in Fig. 14a). This finding deserves careful consideration, since it may have implications for seismic hazard. To this end, we recall some results obtained by Azzaro et al. (2017), who derived a magnitude-size scaling relationship specific for Etna. Briefly, the rupture lengths of these shallow volcano-tectonic earthquakes are differently scaled vs magnitude, ca. 1 order lesser than the purely tectonic events (for instance, a rupture 10 km long is theoretically associated with M_W 5.4 at Etna compared to M_W 6.2–6.6 in tectonic regions). Taking this into account, Fig. 14b shows that the theoretical length for an M_W 4.0 event like the 2009 one, is 2 km, not dissimilar from the value observed in the field (1.9 km) or the one obtained from the source parametrization (2.5 km, i.e. the projection at the surface). Fig. 14c illustrates the maximum magnitude expected for SLF, obtained from the probabilistic approach based on the FiSH code (Pace et al., 2016), reaching the value of 4.8.

Now, using this value for calculating the associated earthquake rupture length, we obtain a 5 km long fault. This result is consistent with the overall extension of the seismogenic segment of SLF, represented by the summation of the grey and white sections in Fig. 14a. In other words, the 2009 aftershocks may represent the initial stage of the fault propagation towards the north.

7. Conclusions

This work presents a detailed multidisciplinary analysis aimed at constraining a model of behaviour for the San Leonardello fault, a structure in the eastern flank of Mt. Etna volcano characterised by frequent seismicity and aseismic creep. In this case-study, we demonstrate that multidisciplinary data collected for volcano surveillance offer an opportunity also to investigate the dynamics of faults, revealing how deformation affects different sections of the same structure both in space and time.

By comparing and integrating independent approaches - field observations, seismological and satellite (GNSS, InSAR) datasets - we were able to recognise different deformative episodes accompanying the fault activity in 2009 and 2016, also at the scale of the seismic source.

The main findings, validated by the full coherence of data, are as follows:

- the San Leonardello fault is a segmented feature characterised by stick-slip, seismogenic behaviour in the northern section and stable-sliding behaviour in the southern one;
- the two fault segments are separated by a persistent barrier hampering earthquake ruptures to propagate southwards;
- the main historical earthquakes are always accompanied by an increase of the creep-rate along the southern segment;
- the 2009 seismic sequence was extremely shallow (< 1 km); the circular source model of the M_W 4.0 mainshock has a radius of 1.3 km; its intersection with the topographic surface produces a 2.5 km long rupture, consistent with the extension of the maximum deformation area detected by InSAR (2.8 km) and surface faulting
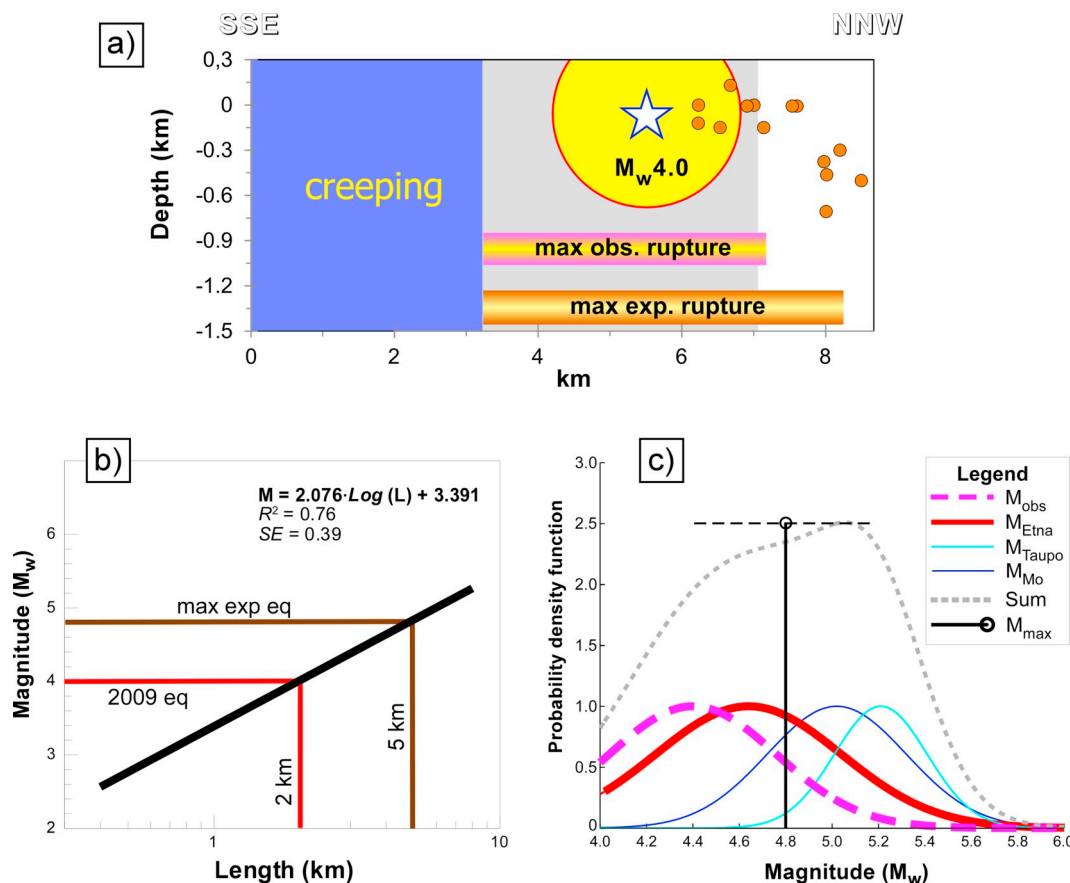
Fig. 14. (a) Conceptual model of behaviour of the San Leonardello fault. The seismogenic segment hosts the M_W 4 event (star) occurring on 13 May 2009, and the associated aftershocks (circles); the extension of maximum historical coseismic surface faulting is also reported. (b) Plot of earthquake magnitude vs. rupture length for the Etna volcano-tectonic earthquakes. The theoretical values of fault lengths for M_W 4 (2009 eq) and 4.8 (max potential eq), are also shown. (c) Maximum expected magnitude (M_{max}) estimated for SLF (for details see Azzaro et al., 2017). Abbreviations: M_{obs}, maximum observed magnitude; M_{etna} - M_{Taupo}, magnitude from earthquake scaling relationships for the Etna and Taupo (New Zealand) volcanic regions; M_{Mo}, scalar seismic moment magnitude; Sum, summation of the probability density functions; M_{max}, central value of the Gaussian fit and associated standard deviation (horizontal dashed line).

(1.9 km);

- the coseismic displacement of the 2009 mainshock has a mean value of ~2.7 cm both from the theoretical source model and InSAR measurements; the maximum offset (net slip) measured in the field by InSAR and GNSS data, is in the range 5–6 cm; kinematics is normal faulting with dextral component of movement;
- the short-term fault displacement measured by InSAR during the April–May 2009 activity shows the same pattern of the long-term cumulative offset of the fault scarp, suggesting that we managed to grasp the basic process of fault growth;
- the stress drop ($\Delta\sigma$) related to the M_W 4.0 earthquake, ~0.2 MPa, is lower than the one obtained for events with the same magnitude in tectonic domains, and can be explained by the shallowness of the source. Values of $\Delta\sigma$ < 2 MPa are reported in areas characterised by the occurrence of slow slip events or low frequency earthquakes;
- the maximum expected magnitude (potential earthquake) is equal to M_W 4.8, needing 5 km of fault to be ruptured; this value is consistent with the overall length of the San Leonardello fault, taking into account the northernmost tip tracked by the 2009 aftershocks; from this standpoint, they may represent a step in the tectonic process of fault propagation.

Mt. Etna confirms its role as a perfect natural laboratory for testing methodologies and approaches applied also to active faults, shedding light on tectonic processes which appear invariant at large and small scales. Given the number of faults characterised by stick-slip vs. stable sliding behaviour at Etna, we believe that other similar studies will help clarify the role of creeping faults in causing earthquakes, and contribute to a better understanding of the seismogenic process.

Declaration of Competing Interest

The authors declare that they have no known competing financial interests or personal relationships that could have appeared to influence the work reported in this paper.

Appendix A. Supplementary data

Supplementary data to this article can be found online at https://doi.org/10.1016/j.tecto.2020.228554.

References

Abercrombie, R.E., 1995. Earthquake source scaling relationships from −1 to 5 ML using seismograms recorded at 2.5-km depth. J. Geophys. Res. 100, 24015–24036.

Alparone, S., Cocina, O., Gambino, S., Mostaccio, A., Spampinato, S., Tuvè, T., Ursino, A., 2013a. Seismological features of the Pernicana-Provenzana fault system (Mt. Etna, Italy) and implications for the dynamics of northeastern flank of the volcano. J. Volc. Geotherm. Res. 251, 16–26.

Alparone, S., D'Amico, S., Gambino, S., Maiolino, V., 2013b. Buried active faults in the Zafferana Etnea territory (south-eastern flank of Mt. Etna): geometry and kinematics by earthquake relocation and focal mechanisms. Ann. Geophys. 56 (1). https://doi.org/10.4401/ag-5758.

Alparone, S., Maiolino, V., Mostaccio, A., Scaltrito, A., Ursino, A., Barberi, G., D'Amico, S., Di Grazia, G., Giampiccolo, E., Musumeci, C., Scarfì, L., Zuccarello, L., 2015. Instrumental seismic catalogue of Mt Etna earthquakes (Sicily, Italy): ten years (2000−2010) of instrumental recordings. Ann. Geophys. 58 (4), S0435. https://doi.org/10.4401/ag-6591.

Avouac, J.P., 2015. From geodetic imaging of seismic and aseismic fault slip to dynamic modeling of the seismic cycle. Annu. Rev. Earth Planet. Sci. 43, 233–271.

Azzaro, R., 1999. Earthquake surface faulting at Mount Etna volcano (Sicily) and implications for active tectonics. J. Geodyn. 28, 193–213.

Azzaro, R., 2004. Seismicity and active tectonics in the Etna region: constraints for a seismotectonic model. In: Bonaccorso, A., Calvari, S., Coltelli, M., Del Negro, C., Falsaperla, S. (Eds.), Mt. Etna: Volcano Laboratory. Am. Geophys. Union, Geophysical Monograph. 143. pp. 205–220.

Azzaro, R., D'Amico, S., 2019. Catalogo Macrosismico dei Terremoti Etnei (CMTE). Istituto Nazionale di Geofisica e Vulcanologia (INGV) https://doi.org/10.13127/cmte. (accessed 16 April 2020).

Azzaro, R., Mattia, M., Puglisi, G., 2001. Fault creep and kinematics of the eastern segment of the Pernicana Fault (Mt. Etna, Italy) derived from geodetic observation and their tectonic significance. Tectonophysics 333, 401–415.

Azzaro, R., D'Amico, S., Tuvè, T., 2011. Estimating the magnitude of historical earthquakes from macroseismic intensity data: new relationships for the volcanic region of Mount Etna (Italy). Seism. Res. Lett. 82 (4), 520–531.

Azzaro, R., Branca, S., Gwinner, K., Coltelli, M., 2012. The volcano-tectonic map of Etna volcano, 1:100.000 scale: morphotectonic analysis from high-resolution DEM integrated with geologic, active faulting and seismotectonic data. Ital. J. Geosci. 131 (1), 153–170.

Azzaro, R., Bonforte, A., Branca, S., Guglielmino, F., 2013a. Geometry and kinematics of the fault systems controlling the unstable flank of Etna volcano (Sicily). J. Volc. Geotherm. Res. 251, 5–15.

Azzaro, R., D'Amico, S., Peruzza, L., Tuvè, T., 2013b. Probabilistic seismic hazard at Mt. Etna (Italy): the contribution of local fault activity in mid-term assessment. J. Volc. Geotherm. Res. 251, 158–169.

Azzaro, R., D'Amico, S., Mostaccio, A., Scarfì, L., Tuvè, T., Manni, M., 2014. Terremoti con effetti macrosismici in Sicilia orientale nel periodo Gennaio 2009 - Dicembre 2013. In: Quaderni di Geofisica 120. INGV, Roma 55 pp., ISSN 1590-2595. http://istituto.ingv.it/l-ingv/produzione-scientifica/quaderni-di-geofisica/archivio/quaderni-di-geofisica-2014/.

Azzaro, R., Barberi, G., D'Amico, S., Pace, B., Peruzza, L., Tuvè, T., 2017. When probabilistic seismic hazard climbs volcanoes: the Mt. Etna case, Italy – part 1: model components for sources parametrization, Nat. Hazards Earth Syst. Sci. 17, 1981–1998.

Barreca, G., Bonforte, A., Neri, M., 2013. A GIS tool for integrated hazard evaluation on the faults of Mt. Etna (Sicily). J. Volc. Geotherm. Res. 251, 170–186.

Boatwright, J., 1978. Detailed earthquake analysis of two small New York state earthquakes. Bull. Seism. Soc. Am. 68 (4), 1117–1131.

Boatwright, J., 1980. A spectral theory for circular seismic sources: simple estimates of source dimension, dynamic stress drop and radiated energy. Bull. Seism. Soc. Am. 70 (1), 1–27.

Bonaccorso, A., Currenti, G., Del Negro, C., 2013. Interaction of volcano-tectonic fault with magma storage, intrusion and flank instability: a thirty years study at Mt. Etna volcano. J. Volc. Geotherm. Res. 251, 127–136.

Bonforte, A., Branca, S., Palano, M., 2007. Geometric and kinematic variations along the active Pernicana fault: implication for the dynamics of Mount Etna NE flank (Italy). J. Volc. Geotherm. Res. 160, 210–222.

Bonforte, A., Bonaccorso, A., Guglielmino, F., Palano, M., Puglisi, G., 2008. Feeding system and magma storage beneath Mt. Etna as revealed by recent inflation/deflation cycles. J. Geophys. Res. 113, B05406. https://doi.org/10.1029/2007JB005334.

Bonforte, A., Guglielmino, F., Coltelli, M., Ferretti, A., Puglisi, G., 2011. Structural assessment of Mount Etna volcano from Permanent Scatterers analysis. Geochem. Geosyst. 12, Q02002. https://doi.org/10.1029/2010GC003213.

Bonforte, A., Guglielmino, Puglisi, G., 2013a. Interaction between magma intrusion and flank dynamics at Mt. Etna in 2008, imaged by integrated dense GPS and DInSAR data. Geochem. Geophys. Geosyst. 14, 2818–2835.

Bonforte, A., Carnazzo, A., Gambino, S., Guglielmino, F., Obrizzo, F., Puglisi, G., 2013b. A multidisciplinary study of an active fault crossing urban areas: the Trecastagni Fault at Mt. Etna (Italy). J. Volc. Geotherm. Res. 251, 41–49.

Bonforte, A., Fagone, S., Giardina, C., Genovese, S., Aiesi, G., Calvagna, F., Cantarero, M., Consoli, O., Consoli, S., Guglielmino, F., Puglisi, B., Puglisi, G., Saraceno, B., 2016a. Global positioning system survey data for active seismic and volcanic areas of eastern Sicily, 1994 to 2013. Sci. Data 3, 160062. https://doi.org/10.1038/sdata.2016.62.

Bonforte, A., Fagone, S., Giardina, C., Genovese, S., Aiesi, G., Calvagna, F., Cantarero, M., Consoli, O., Consoli, S., Guglielmino, F., Puglisi, B., Puglisi, G., Saraceno, B., 2016b. Database of GPS data collected by surveys on seismic and volcanic areas of Sicily

(Italy) from 1994 to 2013. In: PANGAEA, https://doi.org/10.1594/PANGAEA.857795.

Bonforte, A., Guglielmino, F., Puglisi, G., 2019. Large dyke intrusion and small eruption: the December 24, 2018 Mt. Etna eruption imaged by Sentinel-1 data. Terra Nova 31, 405–412.

Borgia, A., Lanari, R., Sansosti, E., Tesauro, M., Berardino, P., Fornaro, G., Neri, M., Murray, J., 2000. Actively growing anticlines beneath Catania from the distal motion of Mount Etna's decollement measured by SAR interferometry and GPS. Geophys. Res. Lett. 27 (20), 3409–3412.

Branca, S., Coltelli, M., Groppelli, G., 2011. Geological evolution of a complex basaltic stratovolcano: Mount Etna, Italy. Ital. J. Geosci. 130 (3), 306–317.

Brodsky, E.E., Mori, J., 2007. Creep events slip less than ordinary earthquakes. Geophys. Res. Lett. 34, L16309.

Bruno, V., Mattia, M., Montgomery-Brown, E., Rossi, M., Scandura, D., 2017. Inflation leading to a slow slip event and volcanic unrest at Mount Etna in 2016: insights from CGPS data. Geophys. Res. Lett. 44, 12,141–149.

Currenti, G., Bonaccorso, A., Del Negro, C., Guglielmino, F., Scandura, D., Boschi, E., 2010. FEM-based inversion for heterogeneous fault mechanisms: application at Etna volcano by DInSAR data. Geophys. J. Int. 183, 765–773.

Currenti, G., Solaro, G., Napoli, R., Pepe, A., Bonaccorso, A., Del Negro, C., Sansosti, E., 2012. Modeling of ALOS and COSMO-SkyMed satellite data at Mt Etna: implications on relation between seismic activation of the Pernicana fault system and volcanic unrest. Remote Sens. Environ. 125, 64–72.

D'Amato, D., Pace, B., Di Nicola, L., Stuart, F.M., Visini, F., Azzaro, R., Branca, S., Barfod, D.N., 2017. Holocene slip rate variability along the Pernicana fault system (Mt. Etna, Italy): evidence from offset lava flows. Bull. Geol. Soc. Am. 129 (3–4), 304–317.

De Novellis, V., Atzori, S., De Luca, C., Manzo, M., Valerio, E., Bonano, M., Cardaci, C., Castaldo, R., Di Bucci, D., Manunta, M., Onorato, G., Pepe, S., Solaro, G., Tizzani, P., Zinno, I., Neri, M., Lanari, R., Casu, F., 2019. DInSAR analysis and analytical modeling of Mount Etna displacements: the December 2018 volcano-tectonic crisis. Geophys. Res. Lett. 46, 5817–5827.

Evans, J.R., Eberhart-Phillips, D., Thurber, C.H., 1994. User's manual for SIMULPS12 for Imaging Vp and Vp/Vs: a derivative of the "Thurber" tomographic inversion SIMUL3 for local earthquakes and explosions. USGS Open File Rep. 94–431 (101 pp.).

Froger, J.L., Merle, O., Briole, P., 2001. Active spreading and regional extension of Mount Etna imaged by SAR interferometry. Earth Planet. Sci. Lett. 187, 245–258.

Gambino, S., Bonforte, A., Carnazzo, A., Falzone, G., Ferrari, F., Ferro, A., Guglielmino, F., Laudani, G., Maiolino, V., Puglisi, G., 2011. Displacement across the Trecastagni Fault (Mt. Etna) and induced seismicity: the October 2009 to January 2010 episode. Ann. Geophys. 54 (4), 414–423.

Giampiccolo, E., D'Amico, S., Patanè, D., Gresta, S., 2007. Attenuation and source parameters of shallow microearthquakes at Mt. Etna volcano (Italy). Bull. Seism. Soc. Am. 97, 184–197.

Gresta, S., Bella, D., Musumeci, C., Carveni, P., 1997. Some efforts on active faulting processes (earthquakes and aseismic creep) acting on the eastern flank of Mt. Etna. Acta Vulcanologica 9 (1/2), 101–108.

Gross, F., Krastel, S., Geersen, J., Behrmann, J.H., Ridente, D., Chiocci, F.L., Bialas, J., Papenberg, C., Cukur, D., Urlaub, M., Micallef, A., 2016. The limits of seaward spreading and slope instability at the continental margin offshore Mt. Etna, imaged by high-resolution 2D seismic data. Tectonophysics 667, 63–76.

Grünthal, G., 1998. European macroseismic scale 1998 (EMS-98). In: European Seismological Commission, Subcommission on Engineering Seismology, working Group Macroseismic Scales. 15. Conseil de l'Europe, Cahiers du Centre Européen de Géodynamique et de Séismologie, Luxembourg, pp. 99. http://www.ecgs.lu/cahiers-bleus/.

Guglielmino, F., Bignami, C., Bonforte, A., Briole, P., Obrizzo, F., Puglisi, G., Stramondo, S., Wegmuller, U., 2011. Analysis of satellite and in-situ ground deformation data integrated by the SISTEM approach: the April 3, 2010 earthquake along the Pernicana fault (Mt. Etna - Italy) case study. Earth Planet. Sci. Lett. 312 (3–4), 327–336.

Gwinner, K., Coltelli, M., Flohrer, J., Jaumann, R., Matz, K.D., Marsella, M., Roatsch, T., Scholten, F., Trauthan, F., 2006. The HRSC-AX Mt. Etna project: high-resolution orthoimages and 1 m DEM at regional scale. Int. Arch. Phot. Rem. Sens. XXXVI (Part 1). http://isprs.free.fr/documents/Papers/T05-23.pdf.

Harris, R.A., 2017. Large earthquakes and creeping faults. Rev. Geophys. 55, 169–198.

Hooper, A., 2008. A multi-temporal InSAR method incorporating both persistent scatterer and small baseline approaches. Geophys. Res. Lett. 35, L16302.

Kanamori, H., 1977. The energy release in great earthquakes. J. Geophys. Res. 82, 2981–2987.

Keylis-Borok, V., 1959. On estimation of the displacement in an earthquake source and of source dimensions. Ann. Geophys. 1959 (12), 205–214.

Le Corvec, N., Walter, T.R., Ruch, J., Bonforte, A., Puglisi, G., 2014. Experimental study of the interplay between magmatic rift intrusion and flank instability with application to the 2001 Mount Etna eruption. J. Geophys. Res. 119, 5356–5368. https://doi.org/10.1002/2014JB011224.

Lee, J.C., Angelier, J., Chu, H.-T., Hu, J.-C., Jeng, F.-S., Rau, R.-J., 2003. Active fault creep variations at Chihshang, Taiwan, revealed by creep meter monitoring, 1998–2001. J. Geophys. Res. 108 (B11), 2528. https://doi.org/10.1029/2003JB002394.

Lehner, F.K., Urai, J.L. (Eds.), 2000. Aspects of Tectonic Faulting: In Honour of George Mandl. Springer-Verlag, Berlin Heidelberg.

Lindsey, E.O., Fialko, Y., Bock, Y., Sandwell, D.T., Bilham, R., 2014. Localized and distributed creep along the southern San Andreas Fault. J. Geophys. Res. 119, 7909–7922.

Lo Giudice, E., Rasà, R., 1992. Very shallow earthquakes and brittle deformation in active volcanic areas: the Etnean region as example. Tectonophysics 202, 257–268.

Lundgren, P., Casu, F., Manzo, M., Pepe, A., Berardino, P., Sansosti, E., Lanari, R., 2004.

Gravity and magma induced spreading of Mount Etna volcano revealed by satellite radar interferometry. Geophys. Res. Lett. 31, L04602.

Madariaga, R., 1979. On the relation between seismic moment and stress drop in the presence of stress and strength heterogeneity. J. Geophys. Res. 84, 2243–2250.

Mattia, M., Bruno, V., Caltabiano, T., Cannata, A., Cannavò, F., D'Alessandro, W., Di Grazia, G., Federico, C., Giammanco, S., La Spina, A., Liuzzo, M., Longo, M., Monaco, C., Patanè, D., Salerno, G., 2015. A comprehensive interpretative model of slow slip events on Mt. Etna's eastern flank. Geochem. Geophys. Geosyst. 16, 635–658.

Milana, G., Rovelli, A., De Sortis, A., Calderoni, G., Coco, G., Corrao, M., Marsan, P., 2008. The role of long-period ground motions on magnitude and damage of volcanic earthquakes on Mt. Etna, Italy. Bull. Seism. Soc. Am. 98, 2724–2738.

Monaco, C., Tapponnier, P., Tortorici, L., Gillot, P.Y., 1997. Late Quaternary slip rates on the Acireale-Piedimonte normal faults and tectonic origin of Mt. Etna (Sicily). Earth Planet. Sci. Lett. 147, 125–139.

Obrizzo, F., Pingue, F., Troise, C., De Natale, G., 2001. Coseismic displacements and creeping along the Pernicana fault (Etna, Italy) in the last 17 years: a detailed study of a tectonic structure on a volcano. J. Volc. Geotherm. Res. 109, 109–131.

Pace, B., Visini, F., Peruzza, L., 2016. FiSH: MATLAB tools to turn fault data into seismic hazard models. Seismol. Res. Lett. 87, 374–386.

Palano, M., 2016. Episodic slow slip events and seaward flank motion at Mt. Etna volcano (Italy). J. Volcanol. Geotherm. Res. 324, 8–14.

Patanè, D., Giampiccolo, 2004. Faulting processes and earthquake source parameters at Mount Etna: state of the art and perspectives. In: Bonaccorso, A., Calvari, S., Coltelli, M., Del Negro, C., Falsaperla, S. (Eds.), Mt. Etna: volcano laboratory. Am. Geophys. Union, Geophysical Monograph. 143. pp. 167–189.

Patanè, D., Barberi, G., Cocina, O., De Gori, P., Chiarabba, C., 2006. Time-resolved seismic tomography detects magma intrusions at Mount Etna. Science 313, 821–823.

Peruzza, L., Azzaro, R., Gee, R., D'Amico, S., Langer, H., Lombardo, G., Pace, B., Pagani, M., Panzera, F., Ordaz, M., Suarez, Suarez, Tusa, G., 2017. When probabilistic seismic hazard climbs volcanoes: the Mt. Etna case, Italy – part 2: computational implementation and first results. Nat. Hazards Earth Syst. Sci. 17, 1999–2015.

Poland, M., Peltier, A., Bonforte, A., Puglisi, G., 2017. The spectrum of persistent volcanic flank instability: a review and proposed framework based on Kilauea, Piton de la Fournaise, and Etna. J. Volcanol. Geotherm. Res. 339, 63–80.

Polonia, A., Torelli, L., Artoni, A., Carlini, M., Faccenna, C., Ferranti, L., Gasperini, L., Govers, R., Klaeschen, D., Monaco, C., Neri, G., Nijholt, N., Orecchio, B., Wortel, R., 2016. The Ionian and Alfeo-Etna fault zones: new segments of an evolving plate boundary in the central Mediterranean Sea? Tectonophysics 675, 69–90.

Puglisi, G., Bonforte, A., Ferretti, A., Guglielmino, F., Palano, M., Prati, C., 2008. Dynamics of Mount Etna before, during, and after the July–August 2001 eruption

inferred from GPS and differential synthetic aperture radar interferometry data. J. Geophys. Res. 113, B06405. https://doi.org/10.1029/2006JB004811.

Rasà, R., Azzaro, R., Leonardi, O., 1996. Aseismic creep on faults and flank instability at Mount Etna volcano, Sicily. In: McGuire, W.J., Jones, A.P., Neuberg, J. (Eds.), Volcano Instability on the Earth and Other Planets. 110. Geol. Soc. London, Special Publications, pp. 179–192.

Ruch, J., Pepe, S., Casu, F., Solaro, G., Pepe, A., Acocella, V., Neri, M., Sansosti, E., 2013. Seismo-tectonic behavior of the Pernicana Fault System (Mt Etna): a gauge for volcano flank instability? J. Geophys. Res. 118, 4398–4409.

Saraò, A., Cocina, O., Moratto, L., Scarfì, L., 2016. Earthquake features through the seismic moment tensor. In: Azzaro, R., De Rosa, R. (Eds.), Project V3: Multi-disciplinary Analysis of the Relationships Between Tectonic Structures and Volcanic Activity (Etna, Vulcano-Lipari system). 29. pp. 98–101. Final Report. Miscellanea INGV. https://sites.google.com/a/ingv.it/volcpro2014/.

Scarfì, L., Messina, A., Cassisi, C., 2013. Sicily and Southern Calabria focal mechanism database: a valuable tool for the local and regional stress field determination. Ann. Geophys. 56 (1), D0109. https://doi.org/10.4401/ag-6109.

Solaro, G., Acocella, V., Pepe, S., Ruch, J., Neri, M., Sansosti, E., 2010. Anatomy of an unstable volcano from InSAR: multiple processes affecting flank instability at Mt. Etna, 1994–2008. J. Geophys. Res. 115, B10405. https://doi.org/10.1029/2009JB000820.

Sumy, D.F., Neighbors, C.J., Cochran, E.S., Keranen, K.M., 2017. Low stress drops observed for aftershocks of the 2011 Mw 5.7 Prague, Oklahoma, earthquake. J. Geophys. Res. 122, 3813–3834.

Thomas, M.Y., Avouac, J.-P., Champenois, J., Lee, J.-C., Kuo, L.-C., 2014. Spatiotemporal evolution of seismic and aseismic slip on the Longitudinal Valley Fault, Taiwan. J. Geophys. Res. 119, 5114–5139.

Tusa, G., Langer, H., 2016. Prediction of ground-motion parameters for the volcanic area of Mount Etna. J. Seismol. 20, 1–42.

Urlaub, M., Petersen, F., Gross, F., Bonforte, A., Puglisi, G., Guglielmino, F., Krastel, S., Lange, D., Kopp, H., 2018. Gravitational collapse of Mount Etna Southeastern flank. Sci. Adv. 4. https://doi.org/10.1126/sciadv.aat9700.

Wassermann, J., 2002. Volcano seismology. In: Bormann, P. (Ed.), New Manual of Seismological Observatory Practice (NMSOP), International Association of Seismology and Physics of the Earth's Interior (IASPEI). GeoForschungsZentrum, Potsdam.

Wesson, L.W., 1988. Dynamics of fault creep. J. Geophys. Res. 93 (B8), 8929–8951.

Zollo, A., Orefice, A., Convertito, V., 2014. Source parameter scaling and radiation efficiency of microearthquakes along the Irpinia fault zone in southern Apennines, Italy. J. Geophys. Res. 119, 3256–3275.